Linking serpentinization and weathering of peridotite: A study on the mineralogical and geochemical evolution of the Sta. Cruz nickel laterite deposit, Zambales, Philippines

Karmina Aquino [1,2]*, Carlo Arcilla [2,3], Christian Schardt [4], and Carmela Tupaz [5]

[1] Department of Earth Sciences, Eidgenössische Technische Hochschule Zürich (ETH Zürich) - Sonneggstrasse 5, 8092 Zürich, Switzerland

[2] National Institute of Geological Sciences, University of the Philippines - Diliman, Velasquez St, Diliman, Quezon City 1101, Philippines

[3] Department of Science and Technology - Philippine Nuclear Research Institute, Diliman, Quezon City 1101, Philippines; caloy.arcilla@gmail.com

[4] Artec Umweltpraxis GmbH - Fabrikgasse 2, 08294 Lößnitz, Germany; schardt07@gmail.com

[5] Faculty of the International Resource Sciences, Akita University, Akita 010-8502, Japan; catupaz@gipc.akita-u.ac.jp

* Correspondence: karmina.aquino@erdw.ethz.ch

Abstract: While there are extensive studies on the mineralogy and geochemistry of laterites worldwide, the temporal and spatial mineralogical development of a typical nickel laterite profile is still poorly constrained. In this study, we present a detailed mineralogical and geochemical characterization of samples systematically collected from a nickel laterite profile at the Sta. Cruz nickel laterite deposit, Zambales, Philippines, to describe the temporal and spatial development of the laterite profile. Wavelength-dispersive X-ray fluorescence spectroscopy (WDSXRF), mass balance-element mobility calculations, transmitted and reflected light microscopy, and previously reported results from coupled X-ray diffraction (XRD) and Rietveld refinement analyses, reveal that the laterite profile investigated is composed of two main horizons: the limonite and saprolite zones, separated by a thin transitional zone. The main zones are further subdivided into subzones based primarily on the mineral assemblage and major element chemistry: upper limonite, lower limonite, transitional zone, upper saprolite, and lower saprolite. Late-stage garnierite veins were observed cutting the upper and lower saprolite subzones. Investigation of the structure of goethite within the limonite zone via Rietveld refinement show that the crystallinity of goethite decreases with increasing Ni content and increasing crystallite size. This suggests that upwards through the limonite zone, as goethite ages, its crystallinity increases which possibly results in the removal of Ni from its crystal structure and eventual remobilization to the lower laterite zones. We propose a spatio-temporal model of the formation of the Sta. Cruz laterite consisting of four stages: (1) early-stage alteration, (2) continued serpentinization and volume expansion, (3) late stage serpentinization and incipient oxide formation, and (4) goethite ageing and garnierite formation.

Keywords: Nickel laterites, laterization, serpentinization, weathering, goethite ageing

1. Introduction

Nickel laterite deposits are products of serpentinization and subsequent deep intensive chemical weathering of ultramafic rocks [1–6]. Serpentinization results whenever Mg-silicates, typically olivine and, less commonly, pyroxene, comprising ultramafic rocks react with water to form serpentine, brucite, and/or magnetite via the following generalized reaction:

$$Olivine \pm orthopyroxene + H_2O \rightarrow serpentine \pm brucite + magnetite + H_2. \quad (1)$$
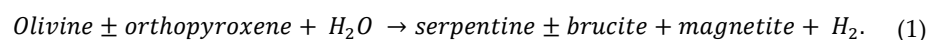
Serpentinization occurs in various tectonic settings wherever water ingress into ultramafic rocks facilitated by fractures or faults is possible, including at/near mid-ocean ridges, subduction forearc regions, fracture zones, and in ophiolite complexes on land [7–13]. Tectonic emplacement of the variably serpentinized ultramafic host rock on land, and subsequent chemical weathering under humid tropical to subtropical conditions results

in the formation of nickel laterite deposits. Nickel laterites typically occur as weathering mantle over ophiolite complexes, as well as komatiites and layered complexes in Archean to Phanerozoic stable cratonic platforms [2,5]. Nickel laterite deposits have a characteristic profile (from the bottom to the top): (1) bedrock consisting of partially altered ultramafics, (2) a silicate or saprolite zone, which holds the highest Ni content and is characterized by Mg-silicates such as serpentine, talc, and garnierite; and (3) an oxide or limonite zone, predominantly composed of iron oxyhydroxides, principally goethite, hematite, and maghemite [1–6].

Serpentinization reactions are associated with the generation of hydrogen, methane, and other short-chain hydrocarbons which provide carbon and energy sources for microbial communities [10,14–19]. Because of this, and the abundance of ultramafic rocks in the Archean Earth [20], serpentinization systems have been important study sites for the biogeochemical origin of life on Earth and even other planets [21,22]. Until recently [e.g., 23,24], most studies about serpentinization focus on the relatively higher temperature (>100°C) processes, while low temperature serpentinization, in particular its relationship and continuity to the chemical weathering of ultramafic rocks exposed on land, have not received as much attention. Complete laterite profiles preserve spatio-temporal information on the mineralogy and geochemistry of these rocks as they undergo serpentinization and weathering of ultramafic rocks and are thus key sites for understanding the link between these two processes.

A recent study [25] emphasizes the primary role of "goethite ageing" with the downward decrease in the bulk Ni content within the limonite of lateritic ores from New Caledonia. Goethite ageing refers to the upward increase in crystallinity of goethite within the limonite zone resulting from the expulsion of Ni from the crystal structure of goethite. Nickel is then either leached from the limonite or is sorbed on the surface of goethite crystals. This is supported by Kuhnel et al. [26] and Trescases [27], who observed a decrease in the crystallinity of goethite with increasing depth. These results suggest that as the nickel laterite profile evolves, goethite crystallinity increases, and nickel content decreases upward through the profile. Goethite ageing is therefore an important aspect of the evolution of the nickel laterite profile.

Here, we investigate samples collected from a nickel laterite profile from the Zambales Ophiolite, Philippines. We aim to describe the evolution of the mineralogy and geochemistry as primary bedrock minerals, such as olivine and orthopyroxene, undergo serpentinization and laterization. In addition, we confirm previous work on goethite ageing [25] and show that small changes in the structure of goethite within the limonite zone is related to its nickel content and to the overall evolution of the laterite profile. We propose a conceptual spatio-temporal model of laterization, highlighting key reactions linking serpentinization and weathering, which will better constrain the genesis of this economically significant deposit.

1.   Zambales Ophiolite Complex

The Zambales ophiolite complex (ZOC), located in Zambales, Philippines (Figure 1), is a generally N-S trending, east dipping complete ophiolite suite comprised of a succession of volcanic rocks, dike-sill complexes, ultramafic and mafic cumulates, residual harzburgite, and lherzolites [28–31]. The ZOC is subdivided into three massifs from north to south: the Masinloc, Cabangan, and San Antonio massifs, with each massif separated by west-northwest fault boundaries [32,33]. The Masinloc massif is made up of two blocks: the Acoje block in the north and the Coto block in the south. The Acoje block and the San Antonio massif are compositionally similar, having an island arc tholeiite (IAT) affinity, whereas the Coto block and the Cabangan massif have a signature transitional from a mid-ocean ridge basalt to island arc (MORB-IA) [29,33]. The ZOC has been dated Eocene, based on the fossil assemblage of the overlying Aksitero formation [34,35]. Direct radiometric dating of various units from the ZOC concurs with the Late Eocene age of the Aksitero formation and yielded a Middle Eocene age for the ophiolite [36,37]. Schweller

et al. [38] suggest an early Miocene eastward tilting and erosion of the ZOC, likely related to the subduction initiation along the ancestral Manila Trench. The Eocene age of the ophiolite implies that it is 10-15 Ma years older than the South China Sea (SCS) crust [39], suggesting that it cannot originate from the SCS [36].
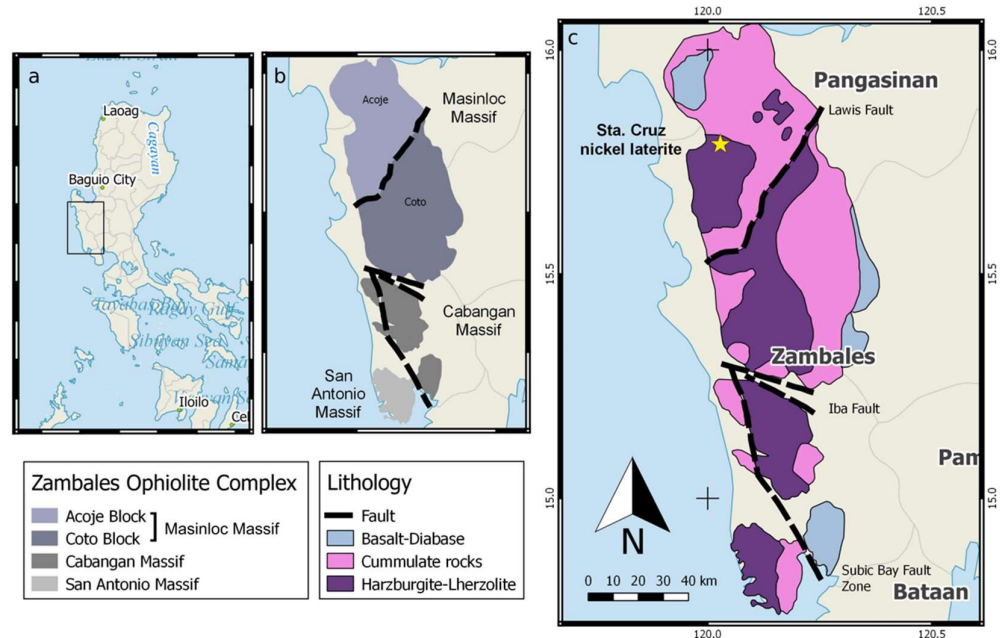
Figure 1. Location of the study area. (**a**) The Zambales Ophiolite Complex is in west Central Luzon, Philippines. (**b**) It is subdivided into three massifs, the Masinloc, Cabangan, and San Antonio Massifs separated by west-northwest fault boundaries. The Masinloc massif is subdivided into the Acoje and Coto Blocks. (**c**) Location of the Sta. Cruz nickel laterite deposit. Reprinted from Aquino et al. [40] (with permission from JGSP).

2.   Sta. Cruz nickel laterite deposit

The Sta. Cruz nickel laterite deposit formed from the weathering of the ultramafic massif of the ZOC Acoje block (Figure 1). The selected nickel laterite profile is located in the municipality of Santa Cruz, in northern Zambales. The deposit exhibits a typical laterite zonation, consisting of an upper limonite layer, which is underlain by the saprolite layer, and bedrock. Nickel mineralization in the deposit is associated with the low Ni, high Fe limonite zone and the low Fe, high Ni saprolite zone [41]. The underlying bedrock is harzburgite with sporadic dunite lenses and minor chromite.

The nickel laterite profile investigated (Figure 2) is approximately 12 m high and composed of two main units - an upper limonite zone (~7 m), and a lower saprolite zone (~5 m), as well as a thin transitional zone (~10 cm), each characterized by a distinct set of physical, mineralogical, and geochemical properties. The detailed mineralogy of this outcrop can be found elsewhere [40,42] and is summarized here. The main laterite zones can be further subdivided into five subzones based on the mineralogy (Figure 3). The topmost zone is the upper limonite subzone, dominated by goethite (83-96 wt%) with minor hematite (4-17 wt%). This is underlain by the lower limonite subzone composed of goethite (92-96 wt%) and chromite (4-8 wt%). Similarly, the saprolite zone, which is marked by the dominance of Mg-silicates and a decrease in the abundance of goethite (5-12 wt%), is also subdivided into the upper and lower saprolite subzones. The upper saprolite subzone is comprised mostly of serpentine (64-91 wt%), with minor chlorite (17 wt%) and tremolite (0-8 wt%), while the lower saprolite subzone is distinguished by the presence of relict olivine (20-25 wt%). The transitional zone is a thin layer representing the

mineralogical boundary between the limonite and the saprolite zone. It is marked by the first appearance of silicate minerals and a decrease in goethite abundance to about 80 wt%. The sample taken at a depth of 10.5 m represents the least altered rock in the profile. This sample is moderately serpentinized (~40%) and has significant primary minerals, including 50% olivine, 10% pyroxene, and trace amounts of chromite. Lastly, garnierite veins, composed of about 90 wt% serpentine and 10 wt% goethite, were observed cutting the lower and upper saprolite subzones.
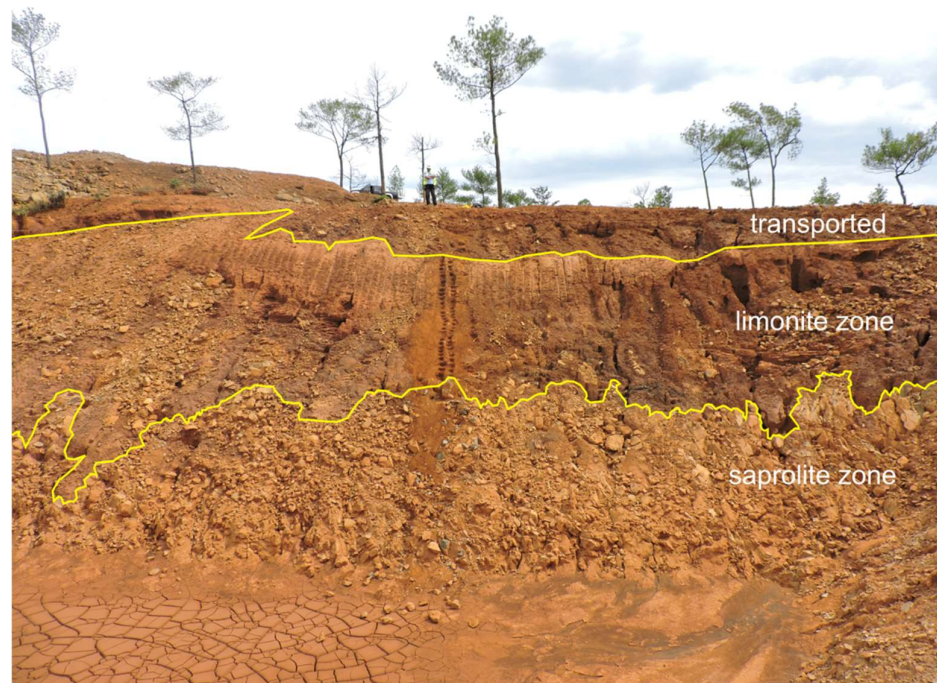
Figure 2. Photo of the nickel laterite profile investigated. The saprolite zone is overlain by the limonite zone. The top most unit is a mechanically transported layer and is therefore not sampled for this study. Reprinted from Aquino et al. [40] (with permission from JGSP).

3.   Materials and Methods

Soil samples from the limonite and transitional zones and rock samples from the saprolite zone were collected from the nickel laterite outcrop described above (Figure 2). The topmost 2 m of the outcrop are composed of mechanically transported materials and were not sampled for this study. Depths shown in Figure 3 and discussed throughout this paper is measured with respect to the top of the upper limonite zone. A total of 33 soil samples were collected at an interval of 20 cm, while 13 rock samples were collected at an interval of 50 cm. Samples collected near the transition zone between the limonite and saprolite zones (i.e., at 6.4 to 6.5 m) were collected at an interval of 10 cm.

3.1.   Petrographic analysis

Eight polished thin sections of the saprolite samples were prepared at the Energy Research and Testing Laboratory at the Philippine Department of Energy. The samples were observed under transmitted and reflected light using a Truevision petrographic microscope and an Olympus BX53P polarizing microscope equipped with DP74 camera at the Earth Materials Science laboratory, National Institute of Geological Sciences.
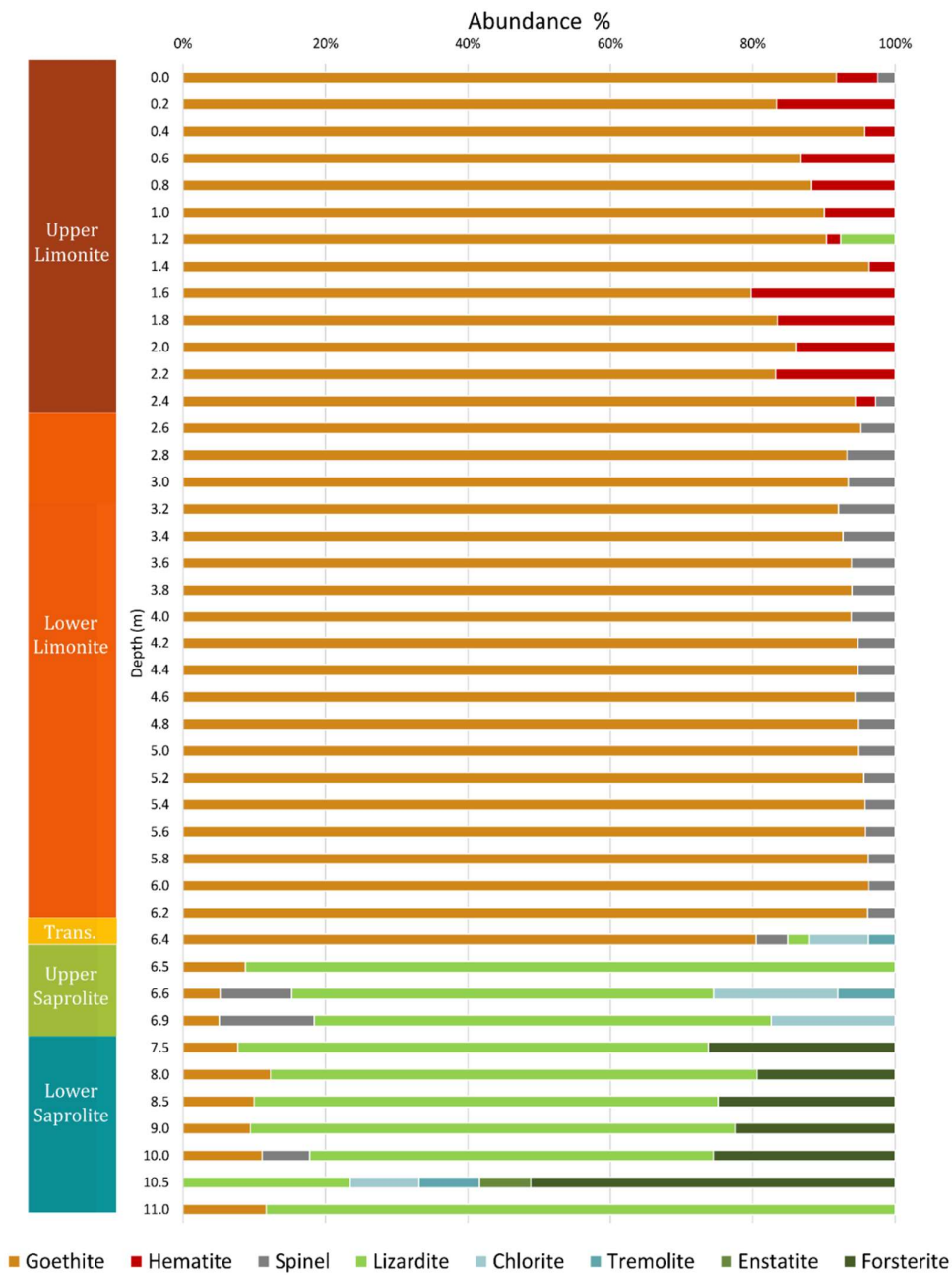
Figure 3. Mineral abundances obtained from Rietveld refinement via Siroquant. Also shown is a schematic diagram showing the corresponding laterite zones based on the mineralogy of the samples. Reprinted from Aquino et al. [40] (with permission from JGSP).

3.2. *X-ray diffraction analysis*

Samples for X-ray diffraction analyses were pulverized to ~200 mesh (<0.075 mm) using an agate mortar and pestle, and subsequently oven-dried at 105C for 24 hours. The powdered samples were then packed on a cylindrical top-filled sample holder. The diffractograms of the samples were determined using a Bragg-Bentano Shimadzu XRD-7000 X-Ray Diffractometer with a CuKα radiation at the National Institute of Geological Sciences. The samples were analyzed using a step size of 1° per min at a 3° to 90° scan range and voltage of 30 kV. The mineral phases were then identified using the PDF4+ Minerals

Database by the International Center for Diffraction Data (ICDD), as well as the Materials Data, Inc. MINERAL database [43]. Mineralogical phases were quantified via Rietveld refinement of the diffractograms using the program Siroquant, version 3.0 [40]. Furthermore, the crystallinity of the goethite phase was evaluated by observing the change in the full width at half maximum (FWHM) of the goethite (110) peak. The FWHM was calculated via the Debye-Scherrer equation:

$$D = \frac{k\lambda}{\beta \cos \theta} \tag{2}$$

where k is a dimensionless shape factor, λ is the wavelength of the X-ray source (1.5418Å for Cu$K\alpha$), D is the crystallite size of goethite phase as obtained from Rietveld refinement, θ is the peak position of the (110) peak in radians, and β is the FWHM.

3.3. Wavelength-dispersive X-ray fluorescence spectroscopy

The samples were pulverized and dried at 105°C for a minimum of 6 hours and then cooled in a desiccator. Fused beads for each sample were then prepared using an AFM - ModuTemp automated fusion machine. The major and minor element concentrations of the samples were analyzed using a PANalytical Axios PW4400 X-Ray Fluorescence Wavelength Dispersive Spectrometer. Preparation of fused beads and XRF analysis were performed at the Intertek Testing Services Philippines, Inc.

3.4. Loss on ignition

Analysis for the loss on ignition (LOI) was performed by Intertek Testing Services Philippines, Inc. Two grams of each sample were weighed on a porcelain crucible and subsequently dried at 105°C for 4 hours to remove the moisture content. The sample was weighed again and then ignited into a furnace at 1000°C for 1 hour. Finally, the sample was weighed again and the %LOI was calculated using the following equation:

$$\% \, LOI = \frac{(m_b - m_c)}{(m_b - m_a)} \times 100 \tag{3}$$

where %LOI is the loss on ignition expressed as wt% of the dry mass, m_a is the mass of the empty crucible, m_b is the mass of the crucible containing the dry mass, and m_c is the mass of the crucible containing the ignited dry mass.

3.5. Mass balance calculations

Quantitative mass balance calculations were performed following the methodology of Venturelli et al. [44]. Relative mass change of a component i, is calculated using the following equation:

$$K_i - 1 = \frac{\Delta M_i}{M_i^R} = \frac{M_i^S}{M_i^R} - 1 \tag{4}$$

where K_i is the mass ratio of component i, M_i^R is the mass of component i in the unaltered rock, and M_i^S is the mass of the same component i in the resulting altered rock. A negative value for the relative mass change (i.e., $K_i - 1 < 0$ or $K_i < 1$) indicates a loss in the component during the conversion of the unaltered rock to the altered rock whereas a positive value for the relative mass change (i. e., $K_i - 1 < 0$ or $K_i < 1$) indicates gain. Given the concentration of component i; in both the altered and unaltered rock (C_i^S and C_i^R, respectively), the mass ratio, K_i can be calculated using the corresponding concentrations of an immobile component, a according to:

$$K_i = \frac{C_i^S C_a^R}{C_i^R C_a^S}. \tag{5}$$

Finally, to calculate the contribution of each component to the associated mass changes, the following equation was used:

$$\frac{\Delta M_i}{M^R} = C_i^R (K_i - 1). \tag{6}$$

3.6. Element mobility determination

The element mobility of each component was evaluated by using the calculated mass ratio (K_i) or relative mass change $(K_i - 1)$ values (Equations 4,5). An immobile component does not change its mass during transformation, and thus the mass ratio value is approximately equal to 1 $(K_i \approx 1 \ or \ K_i - 1 \approx 0)$. Conversely, a mobile component changes mass during transformation, resulting from mass gain or mass loss; thus the absolute value of the mass ratio value is more than one $(|K|_i > 1 \ or \ |K_i - 1| > 0)$. The farther the deviation of the mass ratio value from unity, the more mobile the component is.

3.7. Ultramafic index of alteration

For each sample, an Ultramafic Index of Alteration (UMIA) was calculated following the equation defined by Aiglsperger et al. [45]. This chemical alteration index, which is a modified version of the Mafic Index of Alteration (MIA) by Babechuk et al. [46], as well as other previous chemical alteration indices [47,48], quantifies the chemical changes that occur during the chemical weathering process. Chemical alteration indices calculate the loss of mobile elements with respect to the immobile elements during the chemical weathering of various types of rocks. For the chemical weathering of an ultramafic protolith, where Al$_2$O$_3$ and Fe$_2$O$_3$ are generally immobile and MgO and SiO$_2$ are generally mobile, the UMIA is defined as:

$$\text{UMIA} = 100 \times [(\text{Al}_2\text{O}_3 + \text{Fe}_2\text{O}_{3(T)})/(\text{SiO}_2 + \text{MgO} + \text{Al}_2\text{O}_3 + \text{Fe}_2\text{O}_{3(T)})] \qquad (7)$$

where molar ratios of the respective major elements are used. The following UMIA values are expected for each of the laterite zones: unweathered peridotite bedrock: ~ 3, saprolite: 4-8, limonite: 60-90 [45]. No UMIA values were reported for samples taken from the transition zone.

4. Results

4.1. Petrography

Samples from the limonite and transition zones are extremely weathered with no primary minerals or textures observed in hand specimen (Table 1). The saprolite samples are also heavily weathered and serpentinized in hand specimen and thin section (Figures 4,5). Primary minerals, such as olivine and orthopyroxene, are sparse in most samples except for the least weathered sample, N-1050 (Figure 6). These primary minerals are altered mostly to serpentine (~60-85%), although poorly crystalline Fe oxides (~5-15%) and magnetite (trace), are also present. All samples contain small amounts (<5%) of chromite, except for sample N-690 and N-1000. N-690 is adjacent to a chromitite layer located at depths between 6.8 m and 7.0 m, and thus contains a significant amount of chromite (~20%, Table 2). N-1000 contains visible chromite bands (Figure 4f) in hand specimen. Chromite is a mineral reported to be associated with the peridotite host rock and is therefore of primary origin.

At least three types of serpentine, distinguished by their occurrence and association with secondary magnetite, were observed in the saprolite of the Sta. Cruz nickel laterite deposit. Type 1 serpentine (Figures 5-7) exhibits mesh texture and occurs immediately adjacent to partially or completely dissolved relict olivine grains. It is characteristically magnetite-free, or, when present, magnetite occurs only in minor amounts. Moreover, type 1 serpentine is pale green and slightly pleochroic under plane polarized light and exhibits up to 1st order yellow interference colors in crossed polarized light. Type 2 serpentine, on the other hand, occurs as roughly parallel serpentine veins cross cutting type 1 serpentine and is characteristically magnetite and Fe-oxide stain free. They typically occur in the lower saprolite (e.g., N-900; Figure 6). They are colorless in plane polarized light and exhibits almost black interference colors in crossed polarized light. Type 3 serpentine, like type 2, occurs as veins and is typically observed in the upper saprolite. It is often

associated with moderate to abundant secondary magnetite, which is usually within the core of the serpentinine vein (e.g. N-650; Figure 5). In plane polarized light, type 3 serpentine is colorless to pale greenish yellow and has low relief in crossed polarized light. It exhibits very low interference colors of up to 1ˢᵗ order gray to white.

Table 1 Megascopic description of samples from the limonite and transition zones.

Depth (m)	Zone[1]	Munsell Color	Descriptive	Short description
0	UL	7.5YR 5/8	dark brown	mostly very fine soil (<1 mm) to coarse fragments (> 10 mm) of Fe oxides, poorly sorted
0.8	UL	5YR 4/8	reddish brown	mostly very fine to fine soil (<1 mm) to medium fragments (< 5 mm) of Fe oxides, slightly darker red color probably due to presence of small amounts of hematite
1.6	UL	5YR 4/8	reddish brown	fine to medium (1-5 mm) grained fragments of Fe oxides; slightly darker red color probably due to presence of small amounts of hematite
2.4	UL	5YR 4/8	reddish brown	mostly very fine soil (<1 mm) to coarse fragments (> 10 mm) of Fe oxides; slightly darker red color probably due to presence of small amounts of hematite
3.2	LL	5YR 4/8	reddish brown	mostly medium to coarse grained (5-10 mm) fragments of Fe oxides; slightly darker red color probably due to presence of small amounts of hematite
4.0	LL	7.5YR 5/8	dark brown	fine soil (~1 mm) to medium fragments (< 5 mm) fragments of Fe oxides
4.8	LL	7.5YR 5/8	dark brown	fine soil (~1 mm) to coarse fragments (> 10 mm) of Fe oxides
5.6	LL	7.5YR 5/8	dark brown	mostly medium to coarse grained (5-10 mm) fragments of Fe oxides
6.4	T	7.5YR 5/8	dark brown	poorly sorted mixture of mostly very coarse grained (>30 mm) and medium grained (1-5 mm) Fe oxide-rich rock fragments

[1] UL = upper limonite, LL = lower limonite, T = transition zone.
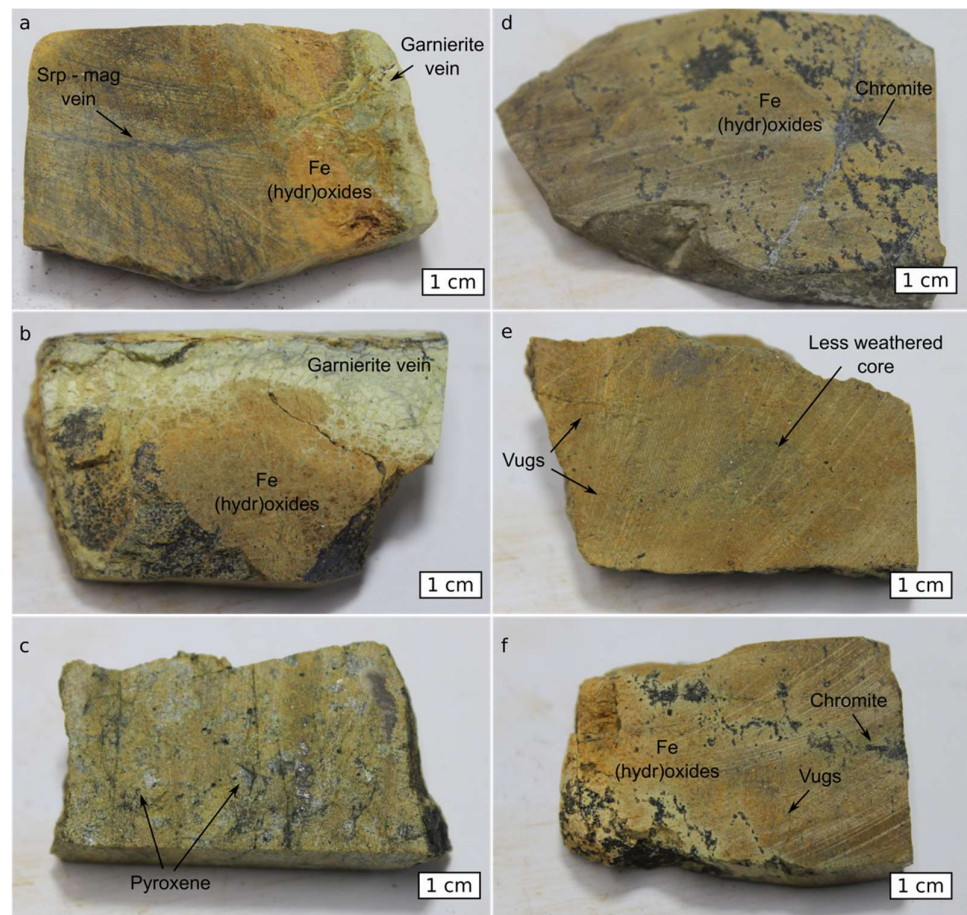
Figure 4. Saprolite samples in hand specimen. (**a**) Sample N-650 (upper garnierite vein/upper saprolite) showing black serpentine-magnetite veins being altered into light green garnierite. (**b**) Sample N-1100 (lower garnierite vein/lower saprolite), heavily altered saprolite sample with a garnierite vein. Note that the garnierite vein emanates from what appear to be boundaries of relict grains. (**c**) Sample N-1050, least altered saprolite sample showing pyroxene crystals about 2-3 mm in size. (**d**) Sample N-690, containing unaltered chromite disseminated in a matrix of strongly weathered to Fe (hydr)oxides. (**e**) Sample N-850, heavily weathered sample with a less altered core. Small dissolution vugs later filled by Fe hydr(oxides) are also present. (**f**) Sample N-1000, showing unaltered disseminated chromite in an Fe hydr(oxide) weathered matrix. Dissolution vugs are also present.

4.1.1. Petrography of upper saprolite samples

Samples from the upper saprolite (e.g., N-650; Figure 5) are strongly weathered and extremely serpentinized (up to 85%). Most of the primary minerals are altered to serpentine, 15% poorly crystalline goethite (amorphous iron oxide), and about 3% magnetite. Primary minerals, including about 5% olivine, 2% tremolite, and trace amounts of orthopyroxenes, are sparse. Olivine crystals, where present, are about 40 to 200 µm in size with average size of about 100 µm, whereas orthopyroxenes are about 200 to 1400 µm in size. Dissolution cavities occur within sites of relict primary minerals (Figure 5). In sample N-660, the size of the cavities are approximately 50 to 300 µm, which are similar in size to the cavities and relict olivine minerals observed in sample N-650R. These cavities are often filled partially or completely with secondary, poorly crystalline goethite ± amorphous silica (Figure 5c-f). Serpentine occurs both as vein-type serpentine (type 3), as well as mesh-type serpentine (type 1) around completely or partially dissolved olivine crystals. In some samples, serpentine exhibits a strong heterogenous and patchy Fe-oxide staining.
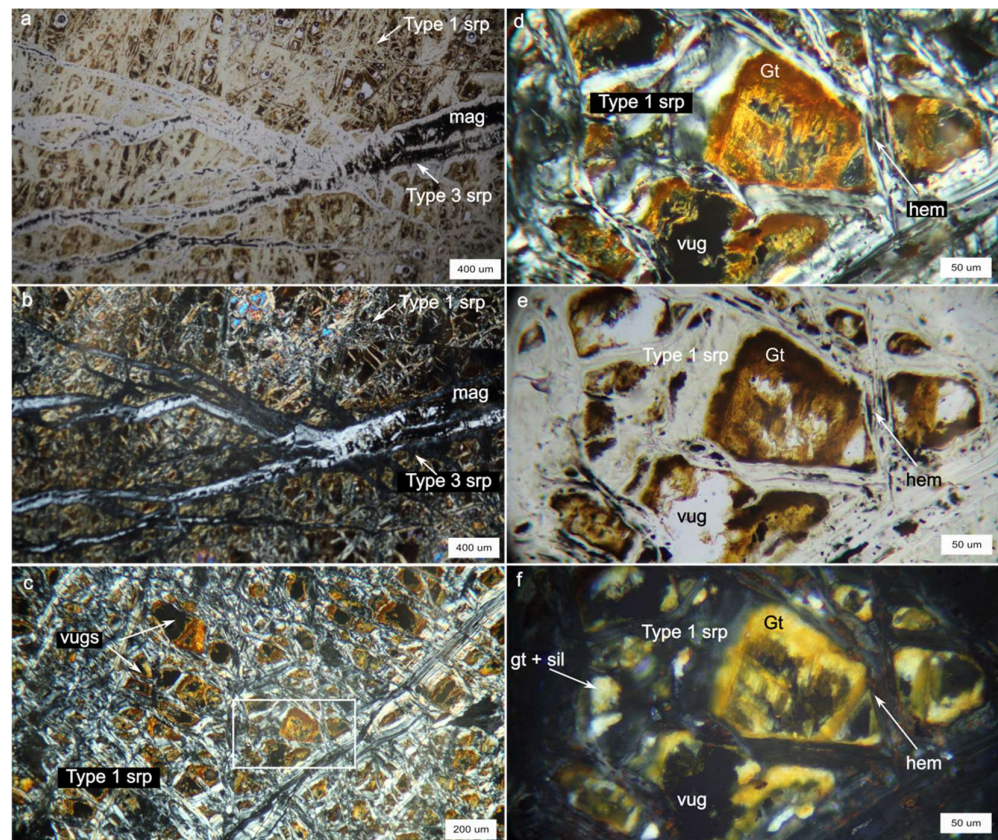
Figure 5. Upper saprolite sample N-650 in thin section. (**a**) Sample N-650 is a heavily serpentinized rock with almost no primary olivine remaining. Type 1 (mesh type) serpentine (srp) surrounding partially of or completely dissolved olivine, crosscut by later Type type 3 (vein type, magnetite-rich) serpentine in plane polarized transmitted light. (**b**) Same as (a) in crossed polarized transmitted light. (**c**) Occurrence of poorly crystalline Fe-oxides (gt), as well as minor amorphous silica (sil), as precipitates within dissolution vugs after olivine, in crossed polarized transmitted light. (**d**) Detail of white box in (c), showing a dissolution vug filled with Fe-oxides. Surrounding mesh serpentine (type 1) contains minor hematite (hem), likely from oxidation of magnetite. (**e**) Same as (c) in plane polarized transmitted light. (**f**) Same as (c) in crossed polarized reflected light, showing bright orange internal reflections of poorly crystalline Fe-oxides, red internal reflections of hematite, and white internal reflections of amorphous silica.

4.1.2. Petrography of lower saprolite samples

Samples from the lower saprolite zone are less serpentinized (~60%) than the upper saprolite samples (Figure 6). Primary minerals, mostly olivine, are more abundant (up to 30%) and occur as 2-4 mm-sized groups of optically continuous crystals, with each individual fragment about 30 to 300 μm in size. Minor minerals include chromite (5%), as well as amorphous Fe oxides, and trace amounts of magnetite. In sample N-750, serpentine occurs both as vein type and mesh type (type 1), with the vein type serpentine associated with fillings of magnetite (type 3). Samples taken from the deeper sections (e.g., N-900) are observed to contain both mesh type (type 1) and magnetite-free, subparallel serpentine veins (type 2) (Figure 6c-d). Throughout the lower saprolite, olivine crystals show dissolution features and, in places, are observed to be directly altered to brown Fe-oxides (Figure 6). Poorly crystalline goethite imparts a generally brown tinge in the lower saprolites sample as a result of either direct replacement of partially dissolved olivine, both as stains in serpentine minerals or infills within dissolution cavities.
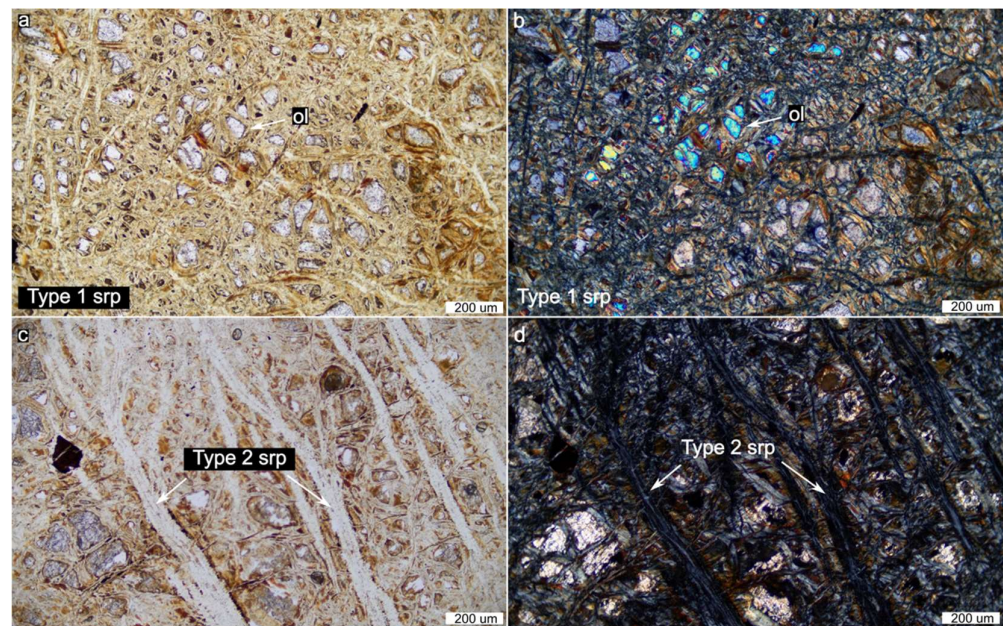
Figure 6. Thin section of samples from the lower saprolite. (**a**) Sample N-750 is strongly serpentin-ized and contains a significant amount of primary olivine fragments in optical continuity. (**b**) Same as (a) in crossed polarized transmitted light. (**c**) N-900 showing roughly parallel serpentine veins (type 2 serpentine) free from Fe-oxide staining. Also shown are partially dissolved relict olivine grains. (**d**) Same as (c) in crossed polarized transmitted light.
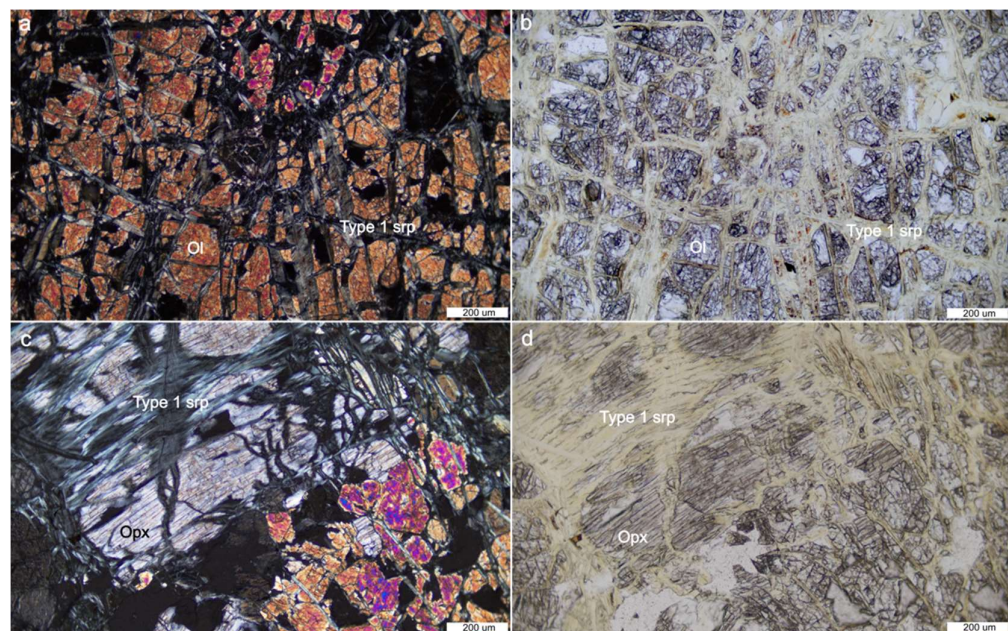
Figure 7. Photomicrographs of the least altered rock in the profile investigated. (**a**) Olivine cut by cross-cutting serpentine veins in transmitted plane polarized light and (**b**) in crossed polarized light. (**c**) Pyroxene is also partially serpentinized parallel to its cleavage planes, in transmitted plane polarized light. (**d**) Same as (c) in crossed polarized transmitted light.

4.1.3. Petrography of the least altered rock

Sample N-1050 represents the least altered rock in the profile (Figure 7). The sample is moderately serpentinized and contains about 40% serpentine but is also composed of abundant primary minerals including about 50% olivine, 10% pyroxene, and trace

amounts of chromite. Olivine is fragmented and is cut by cross cutting vein type serpentine, forming isolated fragments about 100 to 200 μm in size in optically continuous groups of about 2 to 4 mm. The olivine surface is rough and dissolved, as clearly seen in plane polarized transmitted light. Dissolution cavities are also present in the sample and have not yet been filled with any secondary material. Unlike in other samples, olivine crystals are colorless with minimal alteration to Fe-oxides. The serpentine veins are also colorless and do not seem to have Fe-oxide staining. Pyroxene minerals are preserved in this sample and occur as large crystals more than 4 mm in size, often cut by serpentine parallel to cleavage traces (Figure 7).
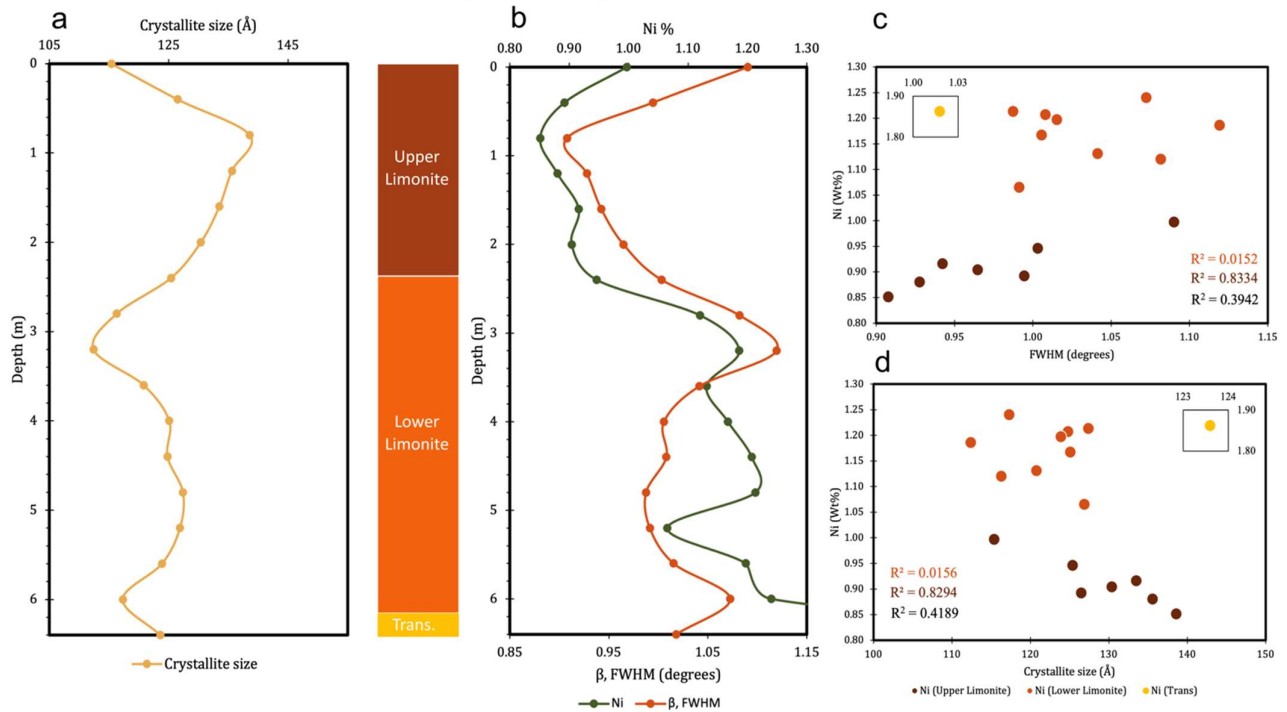
Figure 8. (**a**) Variations in crystallite size of goethite in the limonite and transition zones, as calculated via Rietveld refinement, with depth. (**b**) Bulk Ni content and calculated full-width at half maximum values of goethite in the limonite and transition zones with depth. (**c**) Relationship of bulk Ni content and full-width at half maximum (FWHM) of goethite and (**d**) bulk Ni content and crystallite size of goethite in the limonite and transition zones. Also shown are the R^2 values of the samples from the upper limonite (red), lower limonite (orange), and whole limonite (black) zones.

4.2. Goethite crystallinity and crystallite size measurements

Crystallite size measurements of the goethite phase obtained from Rietveld refinement of the limonite layer reveal a generally decreasing trend with depth (Figure 8a). Goethite crystallite size, which initially increased from 115 to 139 Å in the topmost upper limonite, show a pronounce decreasing trend from 139 to 112 Å in the upper limonite (i.e. depths of 0.8 to 3.2 m). Towards the mid-lower limonite, at depths of 3.6 to 4.8 m, the crystallite size slightly increases in value to 127 Å before it decreased again to 117 Å towards the bottom of the lower limonite. In the transition zone, the value increases again to 124 Å.

The calculated Full-Width at Half Maximum (FWHM) values from the measured crystallite sizes are shown in Figure 8b. As expected from the Debye-Scherrer equation (2), the crystallite size and the FWHM have an inverse relationship. Thus, a generally increasing trend with depth in the FWHM values is observed for the studied limonite samples. FWHM values first decreased slightly from a value of 1.090 degrees at the uppermost limonite layer (0 m) to 0.907 degrees at 0.8 m, and then generally increase to a maximum of 1.112 degrees at a depth of 3.2 m. The FWHM decrease slightly again to 0.987 degrees

at 4.8 m and decrease again up to 1.073 towards the bottom of the lower limonite at a depth of 6.0 m.
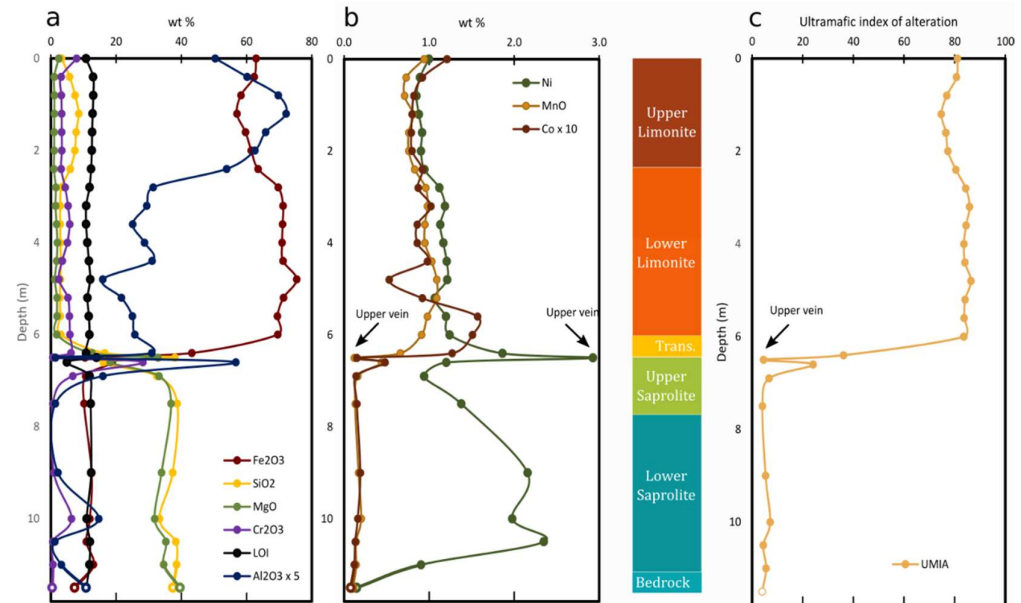
Figure 9. (**a**) Major and (**b**) minor element geochemistry of the studied profile and the corresponding laterite horizons. (**c**) Calculated ultramafic index of alteration (UMIA) as defined by Aiglsperger et al. [45]. Note the relatively high Ni contents and low UMIA of the upper vein.

4.3.   Bulk major and minor geochemistry

4.3.1. Limonite zone

The limonite zone contains elevated Fe_2O_3 (up to 75.4 wt%) and Al_2O_3 (up to 14.4 wt%), and relatively low MgO (average: 1.5 wt%) and SiO_2 (average: 4.5 wt%) concentrations (Table 2, Figure 9a). Within the limonite, Fe content slightly decreases upwards. Interestingly, the Al_2O_3 content of the upper limonite zone is generally higher compared to the lower limonite zone. Within the limonite, the MgO content slightly increases downwards from an average value of 1.2 wt% in the upper limonite to 1.7 wt% in the lower limonite. Contrary to the behavior of MgO values, SiO_2 content shows a decreasing trend downwards within the limonite, with an average value of 6.6 wt% in the upper limonite to 2.9 wt% in the lower limonite. Significant concentrations of Ni, Mn, and Co were noted in the limonite zone of the investigated profile (Figure 9b). Within the limonite, NiO content ranges from 1.1 to 1.6 wt% and generally increase with depth. Average values for MnO and Co are 0.91 and 0.10 wt%, respectively. Both MnO and Co show a slightly increasing trend in the limonite zone with depth. MnO values are enriched up to 1.09 wt% at the lower limonite while Co values are enriched up to 0.16 wt% near the transition zone to the saprolite.

4.3.2. Transition zone, saprolite zone, and garnierite veins

Fe_2O_3 shows a sharp decrease in concentration towards the transition and saprolite zones (average of 43.2 wt% and 12.5 wt%, respectively; Figure 9a). Al_2O_3 content in the transition zone is 6.2 wt%, which decreases further to an average of 3.1 wt% in the saprolite zone. Chromite-rich samples (e.g., N-660; Figure 9a and Table 2) are enriched in Al_2O_3 resulting an apparent spike in Al contents in the upper saprolite zone. From the limonite zone, MgO and SiO_2 increase to values of 12.6 wt% and 16.5 wt%, respectively in the transition zone. The MgO and SiO_2 content of the profile is highly enriched in the saprolite (31.6 wt% and 32.7 wt%, respectively). NiO contents is generally more elevated in the saprolite than in

Table 2. Bulk geochemistry and Ultramafic Index of Alteration (UMIA) of samples from the Sta. Cruz nickel laterite.

Sample	Horizon[1]	Depth	SiO$_2$	TiO$_2$	Al$_2$O$_3$	Fe$_2$O$_3$	Cr$_2$O$_3$	MnO	NiO	Co	MgO	CaO	BaO	Na$_2$O	K$_2$O	P$_2$O5	SO$_3$	LOI	Total	UMIA
N-000	UL	0.0	3.28	0.12	10.08	62.91	7.91	0.94	1.27	0.12	2.42	<0.01	<0.005	<0.01	<0.01	0.01	0.29	10.78	100.0	81.1
N-040	UL	0.4	5.75	0.21	12.03	62.34	3.14	0.73	1.14	0.09	1.02	<0.01	<0.005	0.02	<0.01	0.02	0.39	12.96	99.7	80.8
N-080	UL	0.8	7.43	0.29	13.94	58.27	3.23	0.71	1.08	0.08	1.09	<0.01	<0.005	0.02	0.01	0.02	0.34	13.03	99.5	76.9
N-120	UL	1.2	8.53	0.31	14.42	57.04	3.33	0.81	1.12	0.08	1.07	<0.01	<0.005	<0.01	0.02	0.02	0.30	12.84	99.8	74.7
N-160	UL	1.6	7.74	0.26	13.17	59.67	3.33	0.76	1.17	0.08	1.01	<0.01	<0.005	0.01	0.01	0.02	0.30	12.65	100.1	76.6
N-200	UL	2.0	7.38	0.24	12.51	61.43	3.38	0.76	1.15	0.08	1.04	<0.01	<0.005	<0.01	<0.01	0.01	0.30	12.57	100.8	77.3
N-240	UL	2.4	5.92	0.18	10.78	63.52	3.16	0.83	1.20	0.09	0.95	<0.01	<0.005	0.02	<0.01	0.01	0.24	12.34	99.2	80.5
N-280	LL	2.8	3.27	0.08	6.27	69.67	4.38	0.96	1.43	0.09	1.51	<0.01	0.02	0.02	<0.01	0.01	0.18	11.86	99.7	84.4
N-320	LL	3.2	2.85	0.06	5.88	71.17	5.26	0.98	1.51	0.10	1.42	<0.01	0.01	0.01	<0.01	0.01	0.17	10.84	100.2	85.9
N-360	LL	3.6	2.84	0.06	5.02	71.05	5.76	0.95	1.44	0.09	1.75	<0.01	0.01	0.02	<0.01	0.01	0.15	10.81	99.9	84.5
N-400	LL	4.0	2.90	0.06	5.74	70.90	5.06	0.95	1.49	0.09	1.99	<0.01	<0.005	0.01	<0.01	0.01	0.16	11.19	100.5	83.7
N-440	LL	4.4	3.09	0.07	6.20	71.19	3.49	1.03	1.54	0.10	1.80	<0.01	<0.005	0.02	<0.01	0.01	0.17	11.66	100.3	84.1
N-480	LL	4.8	2.89	0.04	3.18	75.38	2.47	1.09	1.54	0.05	1.24	<0.01	0.06	0.03	<0.01	0.01	0.14	12.07	100.1	86.5
N-520	LL	5.2	2.76	0.06	4.33	71.31	5.24	1.09	1.36	0.09	1.86	<0.01	0.03	0.02	<0.01	0.01	0.12	11.25	99.4	84.2
N-560	LL	5.6	2.86	0.08	5.00	69.43	5.70	0.98	1.52	0.16	1.86	<0.01	<0.005	0.02	<0.01	0.01	0.13	11.65	99.2	83.8
N-600	LL	6.0	3.05	0.08	5.15	69.53	5.85	0.91	1.58	0.15	1.79	0.01	<0.005	<0.01	<0.01	0.01	0.14	11.82	99.9	83.6
N-640	T	6.4	16.48	0.13	6.18	43.23	6.16	0.66	2.37	0.13	12.57	0.65	<0.005	0.04	<0.01	0.01	0.06	10.77	99.3	36.1
N-650	V	6.5	38.04	<0.01	0.29	10.47	0.63	0.12	3.72	0.02	32.87	<0.01	<0.005	<0.01	<0.01	<0.001	0.02	13.98	100.1	4.5
N-660	US	6.6	16.07	0.09	11.34	18.84	*28.16*	0.44	1.53	0.05	18.24	0.16	0.01	0.18	<0.01	<0.001	0.01	4.93	*100*	24.1
N-680	US	6.8	0.71	0.18	19.25	24.35	*42.38*	0.62	0.32	0.05	11.43	<0.01	0.01	0.15	<0.01	<0.001	0.01	0.58	*100*	53.6
N-690	US	6.9	32.52	<0.01	3.19	10.68	6.73	0.16	1.20	0.01	33.16	<0.01	0.01	0.19	<0.01	<0.001	<0.001	11.87	99.7	6.7
N-700	US	7.0	0.91	0.17	18.53	25.00	*41.90*	0.65	0.35	0.06	11.25	<0.01	<0.005	0.18	<0.01	<0.001	0.03	1.04	*100*	53.5
N-750	LS	7.5	38.74	<0.01	0.28	10.16	0.57	0.13	1.75	0.02	36.85	0.02	<0.005	0.01	<0.01	<0.001	0.01	12.20	100.7	4.1
N-900	LS	9.0	37.34	<0.01	0.43	12.51	0.90	0.17	2.75	0.02	33.94	0.01	<0.005	<0.01	<0.01	<0.001	0.01	12.36	100.4	5.3
N-1000	LS	10.0	33.31	0.04	2.93	11.96	6.33	0.20	2.52	0.02	31.83	<0.01	<0.005	<0.01	<0.01	<0.001	0.01	11.01	100.1	7.2
N-1050	LS	10.5	38.27	<0.01	0.25	10.88	0.54	0.14	2.99	0.01	35.29	0.01	<0.005	<0.01	<0.01	<0.001	0.01	11.98	100.4	4.5
N-1100	V	11.0	38.55	0.01	0.64	13.08	0.65	0.14	1.15	0.01	34.60	<0.01	<0.005	<0.01	<0.01	<0.001	0.01	11.82	100.7	5.6

[1] UL = upper limonite, LL = lower limonite, T = transition zone, V = vein, US = upper saprolite, LS = lower saprolite.

* Cr-rich samples with Cr$_2$O$_3$ contents above the detection limit of XRF; Cr$_2$O$_3$ content calculated assuming total wt% = 100 wt%.

All compositions are in wt%

the limonite, with values of up to 3.0 wt% (Figure 9b). MnO and Co values are generally not as significant within the saprolite as in the limonite zone with average values of 0.21 wt% for MnO and 0.02 wt% for Co. Overall, the two garnierite veins have slightly higher SiO_2, MgO, and NiO and lower Fe_2O_3, Al_2O_3, and MnO than the average saprolite (Table 2). Interestingly, the garnierite vein sampled at a higher depth has a higher NiO content than the vein sampled below the lower saprolite. LOI values do not show any significant difference between each laterite horizon, with values ranging from 10.8 to 14.0 wt% within the profile.
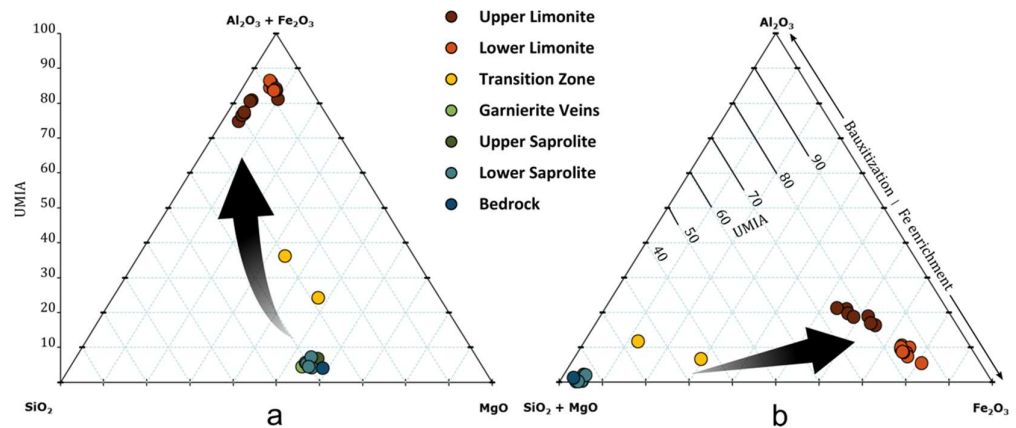
Figure 10. Chemical evolution of the laterite profile during weathering as shown by (**a**) molar ternary $Al_2O_3 + Fe_2O_3$-SiO_2-MgO (AF-S-M) and (**b**) molar ternary Al_2O_3-$SiO_2 + MgO$-Fe_2O_3 (A-SM-F) diagrams. Both diagrams show weathering of an initially Mg- and Si- rich peridotite bedrock towards an Al- and Fe-rich limonite while (b) highlights that Fe-enrichment is predominant in the Sta. Cruz nickel laterite over bauxitization. Also shown is the Ultramafic Index of Alteration (UMIA) as defined by Aiglsperger et al. [45].

4.4. Ultramafic index of alteration

The Ultramafic Index of Alteration (UMIA) values calculated for the Sta. Cruz nickel laterite profile (Table 2, Figure 9c) are generally consistent with expected values [45]. UMIA values in the limonite zone range from 74.7 to 86.5. The upper limonite has slightly lower UMIA values than the lower limonite. Towards the transition zone, the UMIA values decrease to 36.1, before decreasing significantly to values < 8 in the saprolite. There is no significant trend in the UMIA values between the upper and lower saprolite or the garnierite veins.

Figure 10 shows plots of the Sta. Cruz nickel laterite samples in molar ternary AF-S-M ($Al_2O_3 + Fe_2O_3$-SiO_2-MgO) and A-SM-F (Al_2O_3-$SiO_2 + MgO$-Fe_2O_3) diagrams, including their corresponding UMIA values. Both diagrams show weathering of an initially Mg- and Si-rich peridotite bedrock towards an Al- and Fe-rich limonite. Figure 10b highlights Fe-enrichment predominant in the Sta. Cruz nickel laterite compared to bauxitization. This observation is supported by the absence of gibbsite in the investigated samples. Moreover, there is a clear separation of the upper and lower limonite samples in both diagrams, indicating that the upper limonite contains relatively more Al and Si compared to the lower limonite.

4.5. Mass changes and element mobility

The limonite zone is characterized by an almost complete removal of SiO_2 (i.e., up to 97% mass loss) and MgO (up to 100% mass loss) and mass gains of Al_2O_3, Fe_2O_3, MnO, Ni, and Co in the lower limonite (Figure 11). Within the limonite zone, both SiO_2 and MgO loss slightly decrease with depth (Table A1). The transition zone is characterized by a slight decrease in the associated SiO_2 and MgO mass loss and a decrease in the mass gains

for Fe_2O_3, MnO, Ni, and Co. Towards the saprolite zone, almost all components experience significant mass gains. Al_2O_3 mass gains of up to +1170% characterize the upper saprolite, which decrease to +27% towards the lower saprolite zone. The saprolite zones also experience significant mass gains in MgO, SiO_2, Fe_2O_3, MnO, Co, and Ni (up to ~10,000%, listed by increasing associated mass gains).
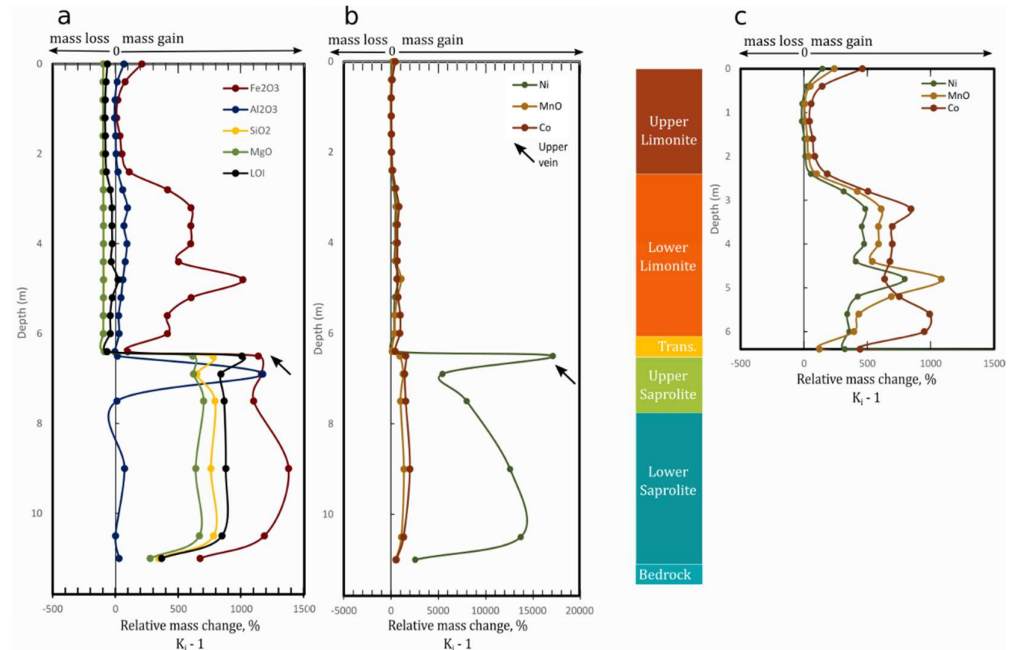
Figure 11. Calculated relative mass change values with respect to initial bedrock concentration (Ki – 1) for the Sta. Cruz nickel laterite profile. Ki – 1 = 0 means that the component does not change its mass during transformation, Ki – 1 > 0 indicates mass gains whereas Ki – 1 < 0 indicates mass loss during transformation. Note the relatively high Ni mass gain associated with the upper vein.

The elements arranged from most to least mobile in the limonite is as follows: Co, Mn, Fe Ni, Mg, Si, Al (Figure 11, Table 3). The mobile elements are generally more mobile in the lower limonite than in the upper limonite, whereas the least mobile elements Mg, Si and Al do not show significant trends with depth. Average element mobility for most of the key elements is one order of magnitude higher in the saprolite than in the limonite zone. In the saprolite, the elements arranged from most to least mobile is Ni, Co, Fe, Mn, Si, Mg, and Al.

5.   Discussion

5.1.   *Laterite zonation*

The Sta. Cruz nickel laterite deposit can be divided into two main zones based on mineralogy, geochemistry, and calculated UMIA: an upper limonite layer and a lower saprolite layer, separated by a transition zone. The transition zone is characterized by mineralogy and geochemistry intermediate between the limonite and saprolite layer. Unfortunately, no fresh bedrock sample was observed in the exposure investigated. The limonite is further subdivided into two layers: upper and lower limonite. Similarly, the saprolite can be divided into upper and lower saprolite zones. Lastly, garnierite serpentine veins were observed cutting the upper and lower saprolite layers.

5.1.1. Limonite zone

The limonite zone represents the most evolved layer of the laterite profile investigated, with a UMIA value of 78. It is an Fe- and Al- rich layer, completely devoid of

primary minerals and made up of the mineral assemblage goethite+hematite for the upper limonite, and goethite+chromite for the lower limonite. Mg and Si are almost completely leached out of this layer with relative mass losses of almost 100%. The upper limonite contains a slightly higher amount of SiO_2 than the lower limonite, resulting in a lower UMIA for the upper limonite. This is probably due to the presence of amorphous silica, a common reaction product of weathering, along with amorphous Fe-oxides. Amorphous silica could not be detected by X-ray diffraction due to the absence of a crystalline structure. Within the limonite, MnO, NiO, and Co generally increase with depth and are enriched in the lower limonite.

Bulk chemistry of the samples reveals a significant amount of Al_2O_3 of more than 10 wt%, although Al-bearing minerals, such as gibbsite, were not observed in the limonite zone. Interestingly, the upper limonite zone has a lower Fe content and higher Al content than the lower limonite zone. The higher Al content in the upper limonite correlates with the occurrence of hematite, which may suggest that Al is hosted in hematite as previously suggested [49,50]. Moreover, goethite with 18% Al substitution best fits the X-ray diffractogram of samples from the upper limonite [42]. Overall, in the absence of mineral chemistry data, it is inferred here that Al is hosted in the limonite by goethite and/or hematite.

We hypothesize that Ni within the limonite is hosted primarily by goethite, with the nickel contents observed to be directly proportional to the FWHM of the goethite (110) peak and inversely proportional to the goethite crystallite size (Figure 8). A stronger correlation ($R^2 = 0.83$) is observed in the upper limonite than in the lower limonite ($R^2 = 0.016$) for both FWHM and crystallite size. Since Ni can substitute for Cr in the chromite crystal structure [51], Ni is likely not exclusively hosted by goethite in lower limonite zone, which contains minor amounts of chromite. Because phases other than goethite host Ni, a weaker correlation between the bulk Ni contents and both goethite crystallite size and FWHM of the goethite (110) peak is observed. The stronger correlation between bulk Ni and goethite crystallinity in the upper limonite support our hypothesis that goethite is the main host of Ni.

5.1.2. Transition zone

The transition zone is a thin layer (~ 6.5 m) between the saprolite and limonite zone and is characterized by an abrupt mineralogical, textural, and geochemical transition from the limonite into the saprolite layer. This layer is comprised of the mineral assemblage goethite+lizardite+chlorite+tremolite+chromite. Goethite is the dominant mineral in the limonite zone whereas lizardite, together with minor amounts of chlorite and tremolite, is characteristic of the saprolite zone. The change in the mineral assemblage in the transition zone is reflected in the geochemistry: abrupt increase in Mg and SiO_2 corresponds to the first appearance of Mg-silicates, decrease in the Fe_2O_3 associated with a decrease in abundance of goethite, and the relatively high Al_2O_3 due to the presence of tremolite and chlorite. The transition zone has an UMIA of 36, a value in between the expected value of at least 60 for limonite zone and the expected value of 4-8 for the saprolite.

Ni in the transition zone is hosted predominantly by goethite, but other phases, such as serpentine and chlorite, may also host Ni. Thus, bulk Ni content cannot be used to determine the effect of Ni content on the structure of goethite in the sample from the transition zone. For both FWHM and crystallite size, the sample from the transition zone is a clear outlier in the generally observed trends.

5.1.3. Saprolite zone

The saprolite zone is comprised mostly of serpentine and has a geochemistry dominated by MgO and SiO_2. The upper saprolite (6.6 to 6.9 m) is composed of the assemblage lizardite+chlorite+chromite+goethite±tremolite. The lower saprolite (7.5 to 11 m) contains a significant amount of primary minerals, mostly olivine, and is made up of the mineral assemblage lizardite+olivine+goethite. Except for the topmost sample from the upper saprolite, samples from the saprolite zone have UMIA values between 4 and 7. Fe is hosted in the saprolite within serpentine, chromite, and poorly crystalline Fe-oxides, occurring

as alteration of olivine and serpentine. Minor amounts of Al_2O_3 in the saprolite suggest the absence of Al-bearing minerals, although small amounts of Al may substitute for Si in the serpentine crystal structure [52,53]. Significant concentrations of Al were observed in saprolite samples containing chlorite.

5.2. *Spatio-temporal evolution of laterization*

Here we present a proposed spatio-temporal model of the formation of the Sta. Cruz nickel laterite deposit, incorporating the results of mineralogical-geochemical investigations presented in this study. Chemical reactions are based on an earlier reactive transport modelling of laterization of the outcrop [42]. The development of the profile is subdivided into four stages (Figure 12) and starts after the emplacement of the Zambales Ophiolite Complex during late Miocene to Plio-Pleistocene [38].
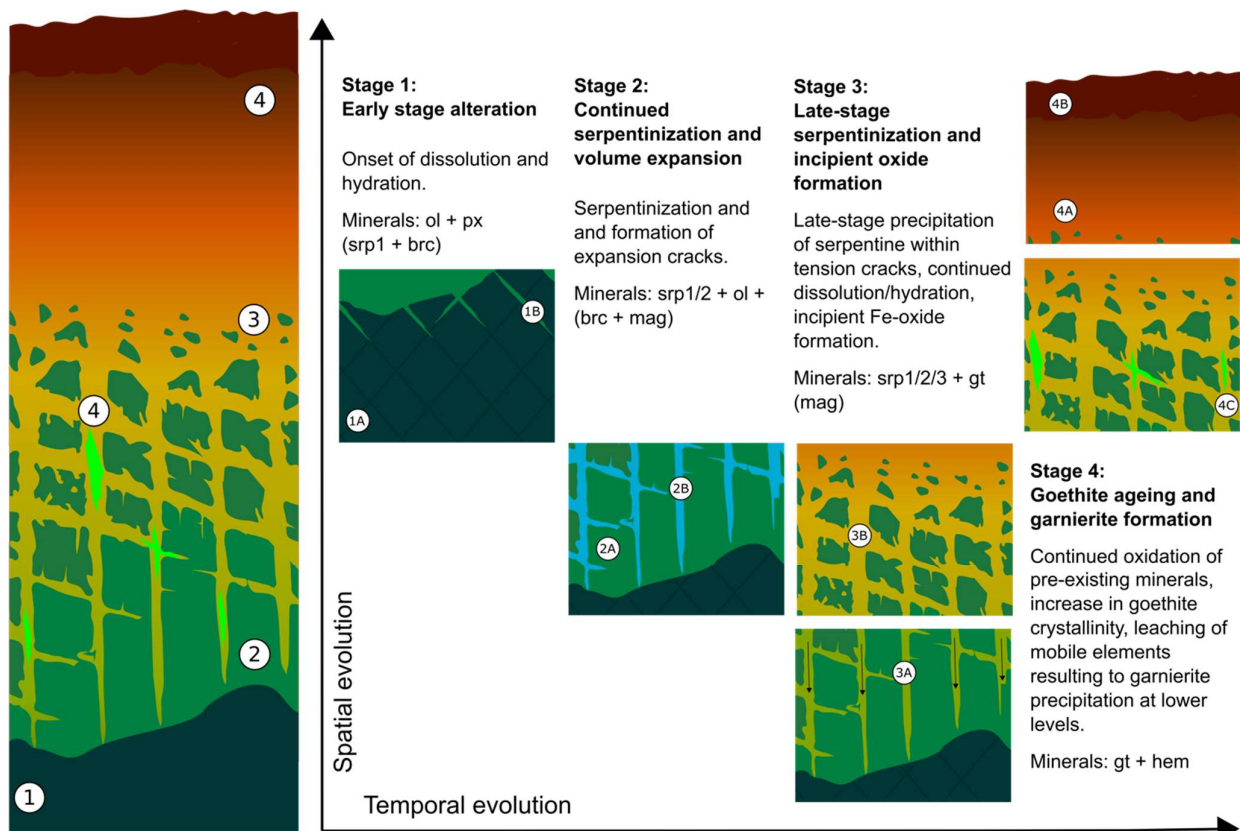
Figure 12. Spatio-temporal model of the formation of the Sta. Cruz laterite profile consisting of 4 stages. During stage 1, fractures introduced during the emplacement of the ZOC provide pathways for rainwater to react with the peridotite protolith (1A). Initial dissolution and hydration (serpentinization) of the primary minerals occur along these fractures (1B). Stage 2 involves continued serpentinization of the primary minerals (2A). Serpentinization is associated with volume expansion that produces expansion cracks at or near the peridotite-serpentinite boundary (2B). Stage 3 is characterized by the precipitation of serpentine within previously formed expansion cracks (3A). Upwards through the profile, continued alteration of primary minerals occurs, as well as the incipient oxidation of pre-existing minerals, forming poorly crystalline Fe-oxide. At the last stage, stage 4, further oxidation of pre-existing minerals forms the limonite zone. Goethite, which is initially poorly crystalline, increases in crystallinity as Ni and other impurities are expelled from its structure (4A). Goethite is also altered to hematite at the topmost part of the profile (4B). Ni and other elements expelled from goethite ageing and hematite formation is leached downwards and contribute to garnierite precipitation in the saprolite zone (4C). ol = olivine, px = pyroxene, srp = serpentine, brc = brucite, mag = magnetite, gt = goethite, hem = hematite.

5.2.1. Stage 1: early stage alteration

The tilting and uplift that led to the emplacement of the ZOC did likely introduce significant fractures and possibly fluid flow pathways into the protolith. Olivine is

unstable at temperatures below ~400°C, and as rainwater is introduced to the system via these fractures and along grain boundaries and cleavage traces, two important processes occur—dissolution and serpentinization (hydration) of primary minerals (Figure 12; stage 1A,1B). The dissolution of olivine and pyroxene can be described by the following reactions:

$$(Mg_xFe_yNi_z)_2SiO_4 + 4\ H+ \longrightarrow 2\ H_2O + 2x\ Mg^{2+} + 2y\ Fe^{2+} + 2z\ Ni^{2+} + SiO_{2(aq)} \tag{8}$$
Olivine

$$(Mg_xFe_yNi_z)SiO_3 + 2\ H+ \longrightarrow H_2O + x\ Mg^{2+} + y\ Fe^{2+} + z\ Ni^{2+} + SiO_{2(aq)}. \tag{9}$$
Pyroxene
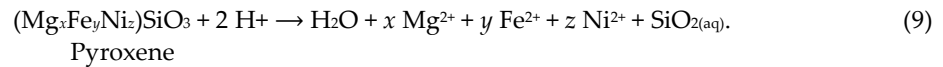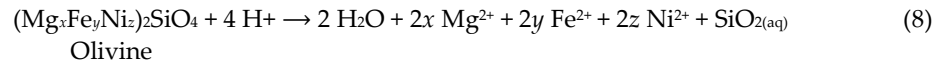
Serpentinization of these minerals, on the other hand, can be described by the reactions:

$$(Mg,Fe,Ni)SiO_3 + 0.67\ H_2O \longrightarrow 0.33\ (Mg,\ Fe,\ Ni)_3Si_2O_5(OH)_4 + 0.33\ SiO_{2(aq)} \tag{10}$$
Pyroxene   Serpentine

$$(Mg,Fe,Ni)_2SiO_4 + 1.33\ H_2O + 0.33\ SiO_{2(aq)} \longrightarrow 0.67\ (Mg,\ Fe,\ Ni)_3Si_2O_5(OH)_4 \tag{11}$$
Olivine   Serpentine

$$(Mg,Fe,Ni)_2SiO_4 + 1.5\ H_2O \longrightarrow 0.5\ (Mg,Fe,Ni)(OH)_2 + 0.5(Mg,Fe,Ni)_3Si_2O_5(OH)_{4.} \tag{12}$$
Olivine   Fe-Brucite   Serpentine
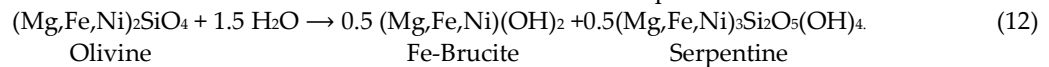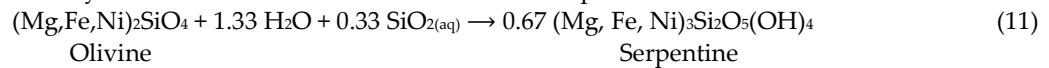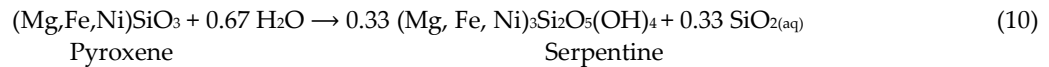
Both dissolution processes as well as the serpentinization of pyroxene (Equations 8-10) can contribute to the initial increase in the $SiO_{2(aq)}$ of the fluid. As suggested by Frost and Beard [54], the initial stages of hydration of olivine takes places by consuming the recently liberated $SiO_{2(aq)}$ in the system (Equations 8-10) to form serpentine (Equation 11). As soon as the $SiO_{2(aq)}$ is exhausted, serpentinization of olivine then proceeds via Equation (12) to form Fe-brucite and serpentine [55–57]. Positive identification of brucite using the analytical techniques we used in this study is difficult or impossible, as brucite can be present cryptically as interlayers within serpentine [58]. Brucite is, however, a widely recognized product of serpentinization [56,57,59]. The Fe-partitioning between the alteration phases brucite and serpentine is complex and affected by various factors, including temperature, initial olivine composition, and water-rock ratio, although the Fe content of brucite during serpentinization increases with decreasing temperature [55]. The early stage serpentinization reaction of olivine and orthopyroxene is generally isochemical (Equations 8-12), consistent with the observed similarity of the ultramafic index of alteration (UMIA) values, calculated from the saprolite and bedrock of the Sta. Cruz laterite deposit. Moreover, initial serpentinization, as recorded in the least altered rock N-1050, typically emanates from grain boundaries forming type 1 serpentine, exhibiting mesh textures around partially or completely dissolved relict olivine (Figure 7). Dissolution cavities were also observed in the primary minerals, implying the rate of dissolution has exceeded the rate of hydration, at least locally.

5.2.2. Stage 2: volume expansion and continued serpentinization

As more water reacts with the partially serpentinized rock, serpentinization reactions (Equations 10-12) proceed further, altering the primary minerals (Figure 12, stage 2A). Over time, serpentine may react with water, producing brucite and $SiO_2(aq)$:

$$(Mg,\ Fe,\ Ni)_3Si_2O_5(OH)_4 + H_2O \longrightarrow 3(Mg,\ Fe,\ Ni)(OH)_2 + 2\ SiO_{2(aq)}. \tag{13}$$
Serpentine   Fe-Brucite
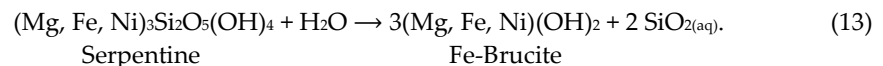
One major consequence of the hydration of peridotite is the associated volume increase that occurs as a rock, composed of dense minerals, is altered to less dense, secondary minerals [60]. Equations 8 to 13 are generally constant-composition reactions, and the decrease in the density of the reaction products will result in an increase in the overall volume of the system. The associated volume expansion can both seal existing fractures in the system and induce new fractures at the same time (Figure 12, stage 2B). At or near the reaction site, the crystallization of higher volume serpentine can seal existing fractures. However, away from serpentine-olivine reaction sites, the force of crystallization and volume

expansion will induce secondary tension cracks [61], adding fluid flow pathways to the system and promoting further reaction with water. These tension cracks were observed in the saprolite zone of the Sta. Cruz laterite profile in the form of roughly parallel type 2 serpentine veins (e.g., N-900, Figure 6). The cracks were formed during continued serpentinization and were later filled by late-stage serpentine, likely formed from fluids leached from the upper horizons.

In addition to serpentine and brucite, abundant magnetite was observed, together with serpentine in samples near the limonite-saprolite boundary (e.g., N-650, Figure 5). Minor amounts of magnetite were also detected, together with both mesh-type and vein-type serpentine from other depths. As suggested earlier [54], at low silica concentrations, magnetite can form from the oxidation of Fe-rich serpentine via:

$$Fe_3Si_2O_5(OH)_4 + 0.5\ O_{2(aq)} \longrightarrow Fe_3O_4 + 2\ SiO_{2(aq)} + 2\ H_2O. \qquad (14)$$
$$\text{Serpentine} \qquad\qquad\qquad \text{Magnetite}$$
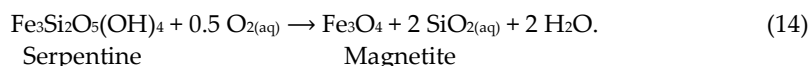
Magnetite is also predicted to form directly from the hydration of olivine; however, this occurs at relatively high temperatures between 250 to 330°C depending on the protolith and water-rock ratios [62]. Instead, we hypothesize that for the Sta. Cruz laterite deposit, very low silica activities drive the oxidation of Fe-serpentine to magnetite.

5.2.3. Stage 3: late stage serpentinization and incipient oxide formation

Volume expansion from the earlier stages of laterite formation resulted in secondary tension cracks away from the peridotite-serpentine reaction front. These cracks introduced secondary fluid pathways to the system and may be filled by late-stage type 3 serpentine veins (Figure 12, stage 3A). Roughly parallel late-stage serpentine veins were observed in the samples adjacent to the least altered rock in the studied profile (e.g., N-900, Figure 6). The serpentine veins were likely formed from solutions leached from the upper horizons of the profile following the reaction:

$$2x\ Mg^{2+} + 2y\ Fe^{2+} + 2z\ Ni^{2+} + 3.33\ H_2O + 1.33\ SiO_{2(aq)} \longrightarrow 0.67\ (Mg_xFe_yNi_z)_3Si_2O_5(OH)_4. \qquad (15)$$
$$\text{Fluid} \qquad\qquad\qquad\qquad \text{Serpentine}$$
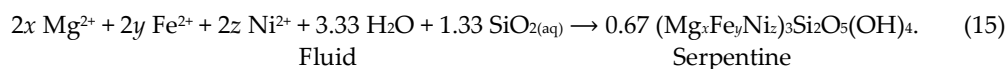
We speculate that further reaction with oxidized rainwater can result in the incipient oxidation of pre-existing minerals in the system to form poorly crystalline goethite in the saprolite zone (Figure 12, stage 3B):

$$(Mg_xFe_y)_2SiO_4 + 4x\ H^+ + \tfrac{2x+3y-2}{2}\ O_{2(aq)} \longrightarrow 2x{-}y\ H_2O + SiO_{2(aq)} + 2x\ Mg^{2+} + 2y\ FeO(OH) \qquad (16)$$
$$\text{Olivine} \qquad\qquad\qquad\qquad\qquad\qquad\qquad \text{Goethite}$$

$$(Mg_xFe_y)_3Si_2O_5(OH)_4 + 6x\ H^+ + \tfrac{6x+9y-8}{4}\ O_{2(aq)} \longrightarrow \tfrac{6x-3y+4}{2}\ H_2O + 2\ SiO_{2(aq)} + 3x{+}\ 3y\ FeO(OH) \qquad (17)$$
$$\text{Serpentine} \qquad\qquad\qquad\qquad\qquad\qquad\qquad \text{Goethite}$$

$$(Mg_xFe_y)(OH)_2 + 2x\ H^+ + \tfrac{2x+3y-2}{4}\ O_{2(aq)} \longrightarrow \tfrac{2x-y+2}{2}\ H_2O + x\ Mg^{2+} + y\ FeO(OH) \qquad (18)$$
$$\text{Fe-brucite} \qquad\qquad\qquad\qquad\qquad\qquad \text{Goethite}$$
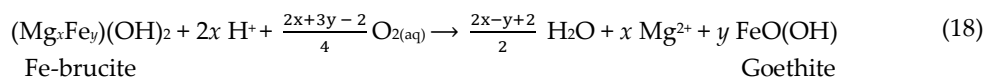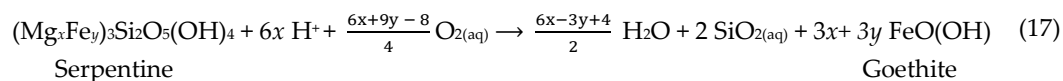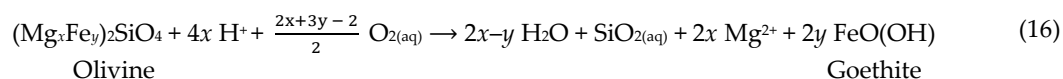
The poor crystallinity of goethite precursor is supported by the absence of well-defined peaks in the diffractogram of the saprolite samples from the Sta. Cruz deposit [40]. Petrographic investigation of saprolites samples revealed that secondary magnetite was altered to hematite, especially at higher depths (e.g., N-650, N-660; Figure 5). In the presence of oxygen, magnetite can be altered to maghemite and then to hematite [50], according to the following reaction:

$$Fe_3O_4 + 0.25\ O_2 \longrightarrow 1.5\ Fe_2O_3 \qquad (19)$$
$$\text{Magnetite} \qquad\qquad \text{Maghemite/Hematite}$$
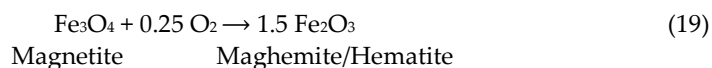
Towards the end of this stage, further dissolution of serpentine and any pre-existing silicates occurs, resulting in an oxide horizon composed dominantly of goethite.

5.2.4. Stage 4: goethite ageing and garnierite formation

The last stage in the formation of the laterite profile involves goethite ageing [25] and the expansion of the limonite zone , accompanied by the formation of later stage garnierite veins at the lower levels (Figure 12, stage 4A,4B). At this stage, most of the silicates formed from the first two stages have already been dissolved or altered to goethite (Equations 16-18). Goethite initially has low crystallinity, as indicated by the absence of distinct peaks in the diffractogram of samples from the saprolite. The poor crystallinity of goethite is attributed to the incorporation of elements, including Ni, that introduces structural defects in the goethite crystal structure [25]. At this stage of laterization, Ni and other impurities are expelled from the structure of goethite, and subsequently leach away towards the lower horizons. The expulsion of Ni from goethite results in goethite ageing or the upward increase in the crystallinity of goethite within the limonite zone as laterization progresses [25,26]. In the Sta. Cruz deposit, goethite ageing is supported by the observed correlation between the bulk Ni content in the limonite and FWHM of the goethite (110) peak. Higher up in the profile, hematite may form from the dehydroxylation of goethite according to:

$$FeO(OH) \rightarrow 0.5\ H_2O + 0.5\ Fe_2O_3. \tag{20}$$
$$\text{Goethite} \qquad\qquad \text{Hematite}$$
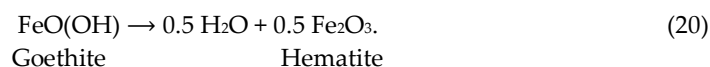
The prevalent silicate dissolution, expulsion of Ni from goethite due to goethite ageing, as well as the likely transformation of Fe-rich brucite to goethite (Equation 18), and subsequently, goethite to hematite (Equation 20), result in the loss of mobile elements, including Mg, Si, and Ni. These elements are leached towards lower horizons, where they form a complex mixture of Ni bearing silicates, mostly Ni-bearing serpentine- or talc-like phases called garnierites [63,64]. The degree and depth of leaching of mobile elements are controlled by the depth of the water table. Above the water table, leaching of mobile elements occurs, while below the water table these mobile elements accumulate and become enriched [6,65]. Elements leached from the upper horizons can also alter the pre-existing secondary minerals in the lower horizon, as described in the reaction below:

$$Mg_3Si_2O_5(OH)_4 + z\ Ni^{2+} \rightarrow (Mg_{1-z}Ni_z)_3Si_2O_5(OH)_4. \tag{21}$$
$$\text{Lizardite} \qquad\qquad \text{Ni-Serpentine (Garnierite)}$$
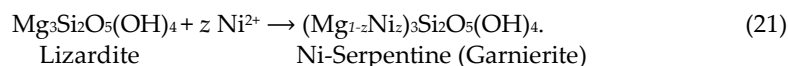
Direct alteration of serpentine to garnierite was observed in the saprolite samples (N-650, N-1100, Figure 4) in serpentine precipitated along secondary cracks.

Over time, the limonite zone expands as oxide-forming reactions (Equations 16-20) continue to progress, deepening the limonite-saprolite zone boundary and increasing the thickness of the limonite zone. The expansion of the limonite zone is affected by a number of factors, including time, the rate of erosion, relief, and climate. A moderate to low-lying relief in a tropical climate provides the ideal conditions for laterite formation. Low to moderate relief results in a limited erosion rate, allowing the preservation of the newly formed limonite zone, and at the same time providing a low-lying water table. Since leaching occurs above the water table, a deep water table allows leaching of a thicker layer of rock and consequently an enhanced supergene Ni enrichment below the water table [1,6].

6.   Conclusions

Combined mineralogical-geochemical analysis revealed that the Sta. Cruz nickel laterite deposit is composed of two main zones, the limonite and saprolite zones, separated by a thin transition zone. Structural investigation of goethite within the limonite zone resulted in a negative correlation between the bulk nickel content and crystallinity of goethite, and between bulk nickel content and crystallite size, emphasizing the important role that goethite plays during the formation of the limonite zone. A spatio-temporal model of

the formation of the Sta. Cruz laterite is composed of four stages, beginning after the emplacement of the Zambales Ophiolite Complex. The first two stages of the formation of the laterite profile are composed of a series of serpentinization reactions affected by the composition of the incoming fluids. We hypothesize that the poorly crystalline Fe-containing brucite, a typical product of serpentinization, is the pre-cursor of goethite, the most significant component of the oxide zone. The model involves a series of reactions that link serpentinization with oxidation reactions, and highlights the key roles of serpentine, Fe-brucite, and goethite in the formation of the nickel laterite profile.

Author Contributions: K.A. conceptualized the study, collected the samples, performed the analyses, and wrote the first draft of the manuscript. C.A. and C.S. supervised the study. C.A. provided resources to conduct the study. C.A., C.S., and C.T. reviewed, revised, and edited the manuscript. All authors have read and agreed to the published version of the manuscript.

Funding: This research received funding from the University of the Philippines – Office of the Vice Chancellor for Research and Development -Thesis and Dissertation Grant and the University of the Philippines - National Institute of Geological Sciences Research Grant to K.A.

Data Availability Statement: Data are contained within the article or in the appendix.

Acknowledgments: Arnulfo Santiago is thanked for welcoming and allowing us to collect the samples used in this study. We also thank Gerald Quiña and Jumar Valdez for their assistance during the fieldwork. James Cesar Refran and James Jimenez are thanked for helping with the photography of the hand samples and thin sections. We also thank the student assistants of the Earth Materials Science laboratories for their assistance in the sample preparation. James Cabreros and Timothy Iringan are acknowledged for their help with some of the figures.

Conflicts of Interest: The authors declare no conflict of interest.

Appendix A

Table A1. Calculated relative mass changes of the samples from the Sta. Cruz laterite.

Sample	Horizon[1]	Depth (m)	SiO_2	Al_2O_3	Fe_2O_3	Cr_2O_3	MnO	NiO	MgO	Co	LOI
N-000	UL	0	-97	67	209	559	240	145	-98	461	-65
N-040	UL	0.4	-97	14	75	50	51	25	-99	144	-76
N-080	UL	0.8	-97	-4	18	11	6	-13	-100	57	-82
N-120	UL	1.2	-97	-7	8	7	13	-16	-100	43	-84
N-160	UL	1.6	-97	1	35	28	27	4	-100	69	-81
N-200	UL	2	-96	4	51	41	38	11	-100	85	-79
N-240	UL	2.4	-96	19	108	76	100	55	-99	184	-73
N-280	LL	2.8	-95	56	413	447	421	313	-98	505	-41
N-320	LL	3.2	-95	95	599	777	609	484	-97	845	-29
N-360	LL	3.6	-95	66	598	860	588	456	-97	697	-29
N-400	LL	4	-94	90	597	744	588	474	-96	697	-26
N-440	LL	4.4	-95	76	500	398	539	409	-97	678	-34
N-480	LL	4.8	-92	58	1011	519	1084	795	-97	637	19
N-520	LL	5.2	-95	44	601	773	689	424	-97	752	-26
N-560	LL	5.6	-96	24	412	612	432	342	-97	991	-42
N-600	LL	6	-96	28	412	632	394	358	-98	949	-42
N-640	T	6.4	-85	-5	96	374	121	323	-90	443	-67
N-650	V	6.5	774	15	1135	1150	942	17176	614	1568	1004
N-690	US	6.9	647	1170	1159	13368	1290	5462	620	1457	837
N-750	LS	7.5	790	11	1098	1048	1029	8036	700	1568	863
N-900	LS	9	758	71	1375	1708	1377	12642	637	2012	876
N-1050	LS	10.5	780	-1	1183	972	1116	13769	666	1345	846
N-1100	V	11	343	27	671	552	508	2575	276	567	367

[1] UL = upper limonite, LL = lower limonite, T = transition zone, V = vein, US = upper saprolite, LS = lower saprolite. Relative mass changes as calculated using equation (4).

References

1. Golightly, J. Nickeliferous laterite deposits. *Econ. Geol.* **1981**, *75th Anniv*, 710–735.
2. Brand, N.W.; Butt, C.R.M.; Elias, M. Nickel Laterites: Classification and Features. *J. Aust. Geol. Geophys.* **1998**, *17*, 81–88.
3. Elias, M. Nickel laterite deposits – geological overview , resources and exploitation. *Giant Ore Depos. Charact. Genes. Explor. CODES Spec. Publ. 4, Hobart, Univ. Tasmania* **2002**, *4*, 205–220.
4. Gleeson, S.A.; Butt, C.R.M.; Elias, M. *SEG Newsletter*. 2003, pp. 1, 12–18.
5. Butt, C.R.M.; Cluzel, D. Nickel laterite ore deposits: Weathered serpentinites. *Elements* **2013**, *9*, 123–128, doi:10.2113/gselements.9.2.123.
6. Golightly, J.P. Progress in understanding the evolution of nickel laterites. *Goldfarb, R.J., Marsh, E. E., Monecke, T., eds., Chall. Find. new Miner. Resour. Metallog. Innov. Explor. new Discov. Soc. Econ. Geol. Spec. Publ.* **2010**, *15*, 451–485.
7. Jöns, N.; Bach, W. *Encyclopedia of Marine Geosciences*; Harff, J., Meschede, M., Petersen, S., Thiede, Jö., Eds.; Encyclopedia of Earth Sciences Series; Springer Netherlands: Dordrecht, 2016; Vol. 20; ISBN 978-94-007-6237-4.
8. Neal, C.; Stanger, G. Past and present serpentinisation of ultramafic rocks: an example from the Semail Ophiolite nappe of northern Oman. *Chem. Weather.* **1985**, 249–247.
9. Kelley, D.S.; Karson, J.A.; Blackman, D.K.; Früh-Green, G.L.; Butterfield, D.A.; Lilley, M.D.; Olson, E.J.; Schrenk, M.O.; Roe, K.K.; Lebon, G.T.; et al. An off-axis hydrothermal vent field near the mid-atlantic ridge at 30° n. *Nature* **2001**, *412*, 145–149, doi:10.1038/35084000.
10. Charlou, J.L.; Donval, J.P.; Fouquet, Y.; Jean-Baptiste, P.; Holm, N. Geochemistry of high H2 and CH4 vent fluids issuing from ultramafic rocks at the Rainbow hydrothermal field (36°14′N,MAR). *Chem. Geol.* **2002**, *191*, 345–359, doi:10.1016/S0009-2541(02)00134-1.
11. Abrajano, T.A.; Sturchio, N.C.; Kennedy, B.M.; Lyon, G.L.; Muehlenbachs, K.; Bohlke, J.K. Geochemistry of reduced gas related to serpentinization of the Zambales ophiolite, Philippines. *Appl. Geochemistry* **1990**, *5*, 625–630, doi:10.1016/0883-2927(90)90060-I.
12. Deschamps, F.; Godard, M.; Guillot, S.; Hattori, K. Lithos Geochemistry of subduction zone serpentinites : A review. *LITHOS* **2013**, *178*, 96–127, doi:10.1016/j.lithos.2013.05.019.
13. Ohara, Y.; Reagan, M.K.; Fujikura, K.; Watanabe, H.; Michibayashi, K.; Ishii, T.; Stern, R.J.; Pujana, I.; Martinez, F.; Girard, G.; et al. A serpentinite-hosted ecosystem in the Southern Mariana Forearc. *Proc. Natl. Acad. Sci. U. S. A.* **2012**, *109*, 2831–2835, doi:10.1073/pnas.1112005109.
14. Kelley, D.S.; Karson, J.A.; Früh-Green, G.L.; Yoerger, D.R.; Shank, T.M.; Butterfield, D.A.; Hayes, J.M.; Schrenk, M.O.; Olson, E.J.; Proskurowski, G.; et al. A serpentinite-hosted ecosystem: The Lost City hydrothermal field. *Science (80-.).* **2005**, *307*, 1428–1434, doi:10.1126/science.1102556.
15. Schmidt, K.; Koschinsky, A.; Garbe-Schönberg, D.; de Carvalho, L.M.; Seifert, R. Geochemistry of hydrothermal fluids from the ultramafic-hosted Logatchev hydrothermal field, 15°N on the Mid-Atlantic Ridge: Temporal and spatial investigation. *Chem. Geol.* **2007**, *242*, 1–21, doi:10.1016/j.chemgeo.2007.01.023.
16. Lang, S.Q.; Butterfield, D.A.; Schulte, M.; Kelley, D.S.; Lilley, M.D. Elevated concentrations of formate , acetate and dissolved organic carbon found at the Lost City hydrothermal field. *Geochim. Cosmochim. Acta* **2010**, *74*, 941–952, doi:10.1016/j.gca.2009.10.045.
17. Monnin, C.; Chavagnac, V.; Boulart, C.; Ménez, B.; Gérard, M.; Gérard, E.; Pisapia, C.; Quéméneur, M.; Erauso, G.; Postec, A.; et al. Fluid chemistry of the low temperature hyperalkaline hydrothermal system of Prony bay (New Caledonia). *Biogeosciences* **2014**, *11*, 5687–5706, doi:10.5194/bg-11-5687-2014.
18. Eickenbusch, P.; Takai, K.; Sissman, O.; Suzuki, S.; Menzies, C.; Sakai, S.; Sansjofre, P.; Tasumi, E.; Bernasconi, S.M.; Glombitza, C.; et al. Origin of short-chain organic acids in serpentinite mud volcanoes of the Mariana convergent margin. *Front. Microbiol.* **2019**, *10*, 1–21, doi:10.3389/fmicb.2019.01729.
19. McCollom, T.M. Geochemical Constraints on Sources of Metabolic Energy for Chemolithoautotrophy in Ultramafic-Hosted Deep-Sea Hydrothermal Systems. *Astrobiology* **2007**, *7*, 933–950, doi:10.1089/ast.2006.0119.
20. Sleep, N.H. The Hadean-Archaean environment. *Cold Spring Harb. Perspect. Biol.* **2010**, *2*, 1–14, doi:10.1101/cshperspect.a002527.
21. Martin, W.; Russell, M.J. On the origin of biochemistry at an alkaline hydrothermal vent. *Philos. Trans. R. Soc. B Biol. Sci.* **2007**, *362*, 1887–1925, doi:10.1098/rstb.2006.1881.
22. Schulte, M.; Blake, D.; Hoehler, T.; McCollom, T. Serpentinization and It's Implication for Life on Early Earth and Mars. *Astrobiology* **2006**, *6*, 364–376.
23. de Obeso, J.C.; Kelemen, P.B. Major element mobility during serpentinization, oxidation and weathering of mantle peridotite at low temperatures. *Philos. Trans. A. Math. Phys. Eng. Sci.* **2020**, *378*, 20180433, doi:10.1098/rsta.2018.0433.
24. Templeton, A.S.; Ellison, E.T.; Glombitza, C.; Morono, Y.; Rempfert, K.R.; Hoehler, T.M.; Zeigler, S.D.; Kraus, E.A.; Spear, J.R.; Nothaft, D.B.; et al. Accessing the Subsurface Biosphere Within Rocks Undergoing Active Low-Temperature Serpentinization in the Samail Ophiolite (Oman Drilling Project). *J. Geophys. Res. Biogeosciences* **2021**, *126*, 1–30, doi:10.1029/2021jg006315.

25. Dublet, G.; Juillot, F.; Morin, G.; Fritsch, E.; Fandeur, D.; Brown, G.E. Goethite aging explains Ni depletion in upper units of ultramafic lateritic ores from New Caledonia. *Geochim. Cosmochim. Acta* **2015**, *160*, 1–15, doi:10.1016/j.gca.2015.03.015.

26. Kuhnel, R.A.; Roorda, H.J.; Steensma, J.J.; Kühnel, R.A.; Roorda, H.J.; Steensma, J.J.; Kuhnel, R.A.; Roorda, H.J.; Steensma, J.J.; Kühnel, R.A.; et al. The crystallinity of minerals-A new variable in pedogenetic processes: A study of goethite and associated silicates in laterites. *Clays Clay Miner.* **1975**, *23*, 349–354, doi:10.1346/CCMN.1975.0230503.

27. Trescases, J.-J. *L'évolution géochimique supergène des roches ultrabasiques en zone tropicale et la formation des gisements nickélifères de Nouvelle-Calédonie*; 1975; Vol. 78; ISBN 2709903628.

28. Abrajano, T.A.; Pasteris, J.D.; Bacuta, G.C. Zambales ophiolite, Philippines I. Geology and petrology of the critical zone of the Acoje massif. *Tectonophysics* **1989**, *168*, 65–100, doi:10.1016/0040-1951(89)90369-7.

29. Hawkins, J.W.; Evans, C. a Geology of the Zambales Range, Luzon, Philippine Islands - ophiolite derived from an island arc-backarc basin pair. *Tecton. Geol. Evol. Southeast Asian seas islands, Part 2 (Hayes, D.E., Ed.) Am. Geophys. Union, Geophys. Monogr. Ser.* **1983**, *27*, 95–123.

30. Rossman, D.L.; Castañada, G.C.; Bacuta, G.C. Geology of the Zambales ophiolite, Luzon, Philippines. *Tectonophysics* **1989**, *168*, doi:10.1016/0040-1951(89)90366-1.

31. Yumul, G.P.; Dimalanta, C.B. Geology of the Southern Zambales Ophiolite Complex, (Philippines): Juxtaposed terranes of diverse origin. *J. Asian Earth Sci.* **1997**, *15*, 413–421, doi:10.1016/S0743-9547(97)00019-6.

32. Bacuta, G.C. Geology of some Alpine-type chromite deposits in the Philippines.pdf. *J. Geol. Soc. Philipp.* **1979**, *33*, 44–80.

33. Yumul, G.P.; Dimalanta, C.B.; Faustino, D. V.; De Jesus, J. V. Translation and docking of an arc terrane: geological and geochemical evidence from the southern Zambales ophiolite complex, Philippines. *Tectonophysics* **1998**, *293*, 255–272, doi:10.1016/S0040-1951(98)00096-1.

34. Garrison, R.E.; Espiritu, E.; Horan, L.J.; Mack, L.E. Petrology, sedimentology, and diagenesis of hemipelagic limestone and tuffaceous turbidites in the Aksitero Formation, central Luzon, Philippines. *U. S. Geol. Surv. Prof. Pap.* **1979**, *1112*, 15–16, doi:-.

35. Amato, F.L. Stratigraphic paleontology in the Philippines. *Philipp. Geol.* **1965**, *19*, 1–24.

36. Fuller, M.; Haston, R.; Almasco, J. Paleomagnetism of the Zambales ophiolite, Luzon, northern Philippines. *Tectonophysics* **1989**, *168*, 171–203, doi:10.1016/0040-1951(89)90375-2.

37. Encarnación, J.P.; Mukasa, S.B.; Obille, E.C. Zircon U-Pb geochronology of the Zambales and Angat Ophiolites, Luzon, Philippines: Evidence for an Eocene arc-back arc pair. *J. Geophys. Res.* **1993**, *98*, 19991, doi:10.1029/93JB02167.

38. Schweller, W.J.; Karig, D.E.; Bachman, S.B. Original Setting and Emplacement History of the Zambales Ophiolite, Luzon, Phillipines, from Stratigraphic Evidence. *Tecton. Geol. Evol. Southeast Asian Seas Islands Part 2* **1983**, *27*, 124–138, doi:10.1029/GM027p0124.

39. Taylor, B.; Hayes, D.E. The tectonic evolution of the South China Basin. *Tecton. Geol. Evol. Southeast Asian seas islands* **1980**, *23*, 89–104.

40. Aquino, K.A.; Arcilla, C.A.; Schardt, C.S. Mineralogical Zonation of the Sta. Cruz Nickel Laterite Deposit, Zambales, Philippines Obtained from Detailed X-Ray Diffraction Coupled with Rietveld Refinement. *J. Geol. Soc. Philipp.* **2019**, *73*, 1–14.

41. Santiago, A.P. de B. Evaluation of Ni-bearing saprolite resources contained in Filipinas Mining Corporation MPSA No. 268-2008-III located Barangay Guinabon, Sta. Cruz, Zambales, Philippines. **2015**.

42. Aquino, K.A. Spatio-temporal evolution of laterization: Insights from detailed mineralogical characterization and reactive transport modelling of Sta. Cruz nickel laterite deposit, Zambales, Philippines, University of the Philippines, 2018.

43. Nickel, E.H.; Nichols, M.C. Mineral database 2003.

44. Venturelli, Giampiero; Contini, Simona; Bonazzi, Achille; Mangia, A. Weathering of Ultramafic Rocks and Element Mobility at Mt. Prinzera, Northern Apennines, Italy. *Mineral. Mag.* **1997**, *61*, 765–778, doi:10.1180/minmag.1997.061.409.02.

45. Aiglsperger, T.; Proenza, J.A.; Lewis, J.F.; Labrador, M.; Svojtka, M.; Rojas-Purón, A.; Longo, F.; Ďurišová, J. Critical metals (REE, Sc, PGE) in Ni laterites from Cuba and the Dominican Republic. *Ore Geol. Rev.* **2016**, *73*, 127–147, doi:10.1016/j.oregeorev.2015.10.010.

46. Babechuk, M.G.; Widdowson, M.; Kamber, B.S. Quantifying chemical weathering intensity and trace element release from two contrasting basalt profiles, Deccan Traps, India. *Chem. Geol.* **2014**, *363*, 56–75, doi:10.1016/j.chemgeo.2013.10.027.

47. Parker, A. An Index of Weathering for Silicate Rocks. *Geol. Mag.* **1970**, *107*, 501–504, doi:10.1017/S0016756800058581.

48. Ohta, T.; Arai, H. Statistical empirical index of chemical weathering in igneous rocks: A new tool for evaluating the degree of weathering. *Chem. Geol.* **2007**, *240*, 280–297, doi:10.1016/j.chemgeo.2007.02.017.

49. Tupaz, C.A.J.; Watanabe, Y.; Sanematsu, K.; Echigo, T. Spectral and chemical studies of iron and manganese oxyhydroxides in laterite developed on ultramafic rocks. *Resour. Geol.* **2021**, *71*, 377–391, doi:10.1111/rge.12272.

50. Cornell, R.M.; Schwertmann, U. *The Iron Oxides: Structure: Properties, reactions, Occurences and Uses*; Wiley-VCH, 2003; ISBN 3527302743.

51. Prince, E. Structure of Nickel Chromite. *J. Appl. Phys.* **1961**, *32*, 1–3, doi:10.1063/1.2000504.

52. Evans, B.W.; Hattori, K.; Baronnet, A. Serpentinite: What, Why, Where? *Elements* **2013**, *9*, 99–106, doi:10.2113/gselements.9.2.99.

53. Rinaudo, C.A.; Gastaldi, D.A. Characterization of Chrysotile, Antigorite, and Lizardite by FT-Raman Spectroscopy. **2003**, *41*, 883–890.

54. Frost, B.R.; Beard, J.S. On Silica Activity and Serpentinization. **2007**, *48*, 1351–1368, doi:10.1093/petrology/egm021.

55.	Klein, F.; Bach, W.; Jöns, N.; McCollom, T.; Moskowitz, B.; Berquó, T. Iron partitioning and hydrogen generation during serpentinization of abyssal peridotites from 15°N on the Mid-Atlantic Ridge. *Geochim. Cosmochim. Acta* **2009**, *73*, 6868–6893, doi:10.1016/j.gca.2009.08.021.

56.	Templeton, A.S.; Ellison, E.T. Formation and loss of metastable brucite: does Fe(II)-bearing brucite support microbial activity in serpentinizing ecosystems? *Philos. Trans. A. Math. Phys. Eng. Sci.* **2020**, *378*, 20180423, doi:10.1098/rsta.2018.0423.

57.	Klein, F.; Humphris, S.E.; Bach, W. Brucite formation and dissolution in oceanic serpentinite. *Geochemical Perspect. Lett.* **2020**, 1–5, doi:10.7185/geochemlet.2035.

58.	Bach, W.; Paulick, H.; Garrido, C.J.; Ildefonse, B.; Meurer, W.P.; Humphris, S.E. Unraveling the sequence of serpentinization reactions: Petrography, mineral chemistry, and petrophysics of serpentinites from MAR 15°N (ODP Leg 209, Site 1274). *Geophys. Res. Lett.* **2006**, *33*, 4–7, doi:10.1029/2006GL025681.

59.	Frost, B.R.; Beard, J.S.; Frost, R.B.; Beard, J.S.; Frost, B.R.; Beard, J.S.; Frost, R.B.; Beard, J.S. On silica activity and serpentinization. *J. Petrol.* **2007**, *48*, 1351–1368, doi:10.1093/petrology/egm021.

60.	Klein, F.; Le Roux, V. Quantifying the volume increase and chemical exchange during serpentinization. *Geology* **2020**, *48*, 552–556, doi:10.1130/G47289.1.

61.	Evans, B.W. The Serpentinite Multisystem Revisited: Chrysotile Is Metastable. *Int. Geol. Rev.* **2004**, *46*, 479–506, doi:10.2747/0020-6814.46.6.479.

62.	Klein, F.; Bach, W.; Mccollom, T.M. Lithos Compositional controls on hydrogen generation during serpentinization of ultrama fi c rocks. *LITHOS* **2013**, *178*, 55–69, doi:10.1016/j.lithos.2013.03.008.

63.	Brindley, G.W. The Nature and Nomenclature of Hydrous Nickel-Containing Silicates. *Clay Miner.* **1974**, *10*, 271–277, doi:10.1180/claymin.1974.010.4.05.

64.	Brindley, G.W.; Hang, P.T.H.I. The Nature of Garnierites - I Structures , Chemical Compositions and Color Characteristics. *Clays Clay Miner.* **1973**, *21*, 27–40.

65.	Freyssinet, P.; Butt, C.R.M.; Morris, R.C.; Piantone, P. Ore-forming processes related to lateritic weathering. *Econ. Geol. 100th Anniv. Vol.* **2005**, *1*, 681–722.